Synthesis, single crystal X-ray, and DFT study of new hybrid-ligand complex [Cu(hfac)_2(Me_3TTF-CH=CH-Pyr)] and new mixed-valence radical ion salt (Me_3TTF-CH=CH-Pyr)_2(PF_6)_3

Hanene Soukehal, Oussama Khaoua, Samira Zeroual, Noura Benbellat, Abdekrim Gouasmia, Stéphane Golhen

Highlights

- Tetrathiafulvalene demonstrates versatility in molecular electronics.
- Experimental and computational methods integrate for a redox-active hybrid.
- Crystal structure analysis exposes a deformed pyramid in Copper (II) complex.
- Noteworthy charge transfer in electronic properties hints at photoelectron conversion suitability.
- Reactivity analysis pinpoints potential attack sites, highlighting sulfur atom reactivity.

Synthesis, Single Crystal X-ray, and DFT study of new hybrid-ligand complex $[Cu(hfac)_2(Me_3TTF\text{-}CH{=}CH\text{-}Pyr)]$ and new mixed-valence radical ion salt $(Me_3TTF\text{-}CH{=}CH\text{-}Pyr)_2(PF_6)_3$

Hanane Soukehal[a], Oussama Khaoua*[a], Samira Zeroual[a], Noura Benbellat*[a], Abdekrim Gouasmia[b] Stéphane Golhen[c].

[a]Laboratoire de Chimie des Matériaux et des Vivants: Activité & Réactivité (LCMVAR), Département de Chimie, Faculté des Sciences de la Matière, Université de Batna-1, Algérie.

[b]Laboratoire des Matériaux Organiques et Hétérochimie, Faculté des sciences et de la technologie, Université Larbi Tébessi, Tébessa, Algérie.

[c]Univ. Rennes, CNRS, ISCR (Institut des Sciences Chimiques de Rennes)−UMR 6226, F-35000 Rennes, France.

Corresponding authors: Noura Benbellat Tel: +213 671214105; Fax: +213 33319015; E-mail addresses:

* noura.benbellat@univ-batna.dz ; oussama.khaoua@univ-batna.dz

Abstract

This paper presents a comprehensive study that combines experimental techniques and Density Functional Theory (DFT) to investigate a newly synthesized mixed-ligand complex, [Cu(hfac)$_2$(Me$_3$TTF-CH=CH-Pyr)] (where hfac is hexafluoroacetylacetonate), and a novel mixed-valence radical ion salt (Me$_3$TTF-CH=CH-Pyr)$_2$(PF$_6$)$_3$. Both are constructed using ligands derived from the tetrathiafulvalene (TTF) donor molecule. These materials are meticulously characterized through single-crystal X-ray diffraction analysis. The complex crystallizes in the monoclinic system, specifically in the C2/c space group, with the following lattice parameters: a = 24.583(2) Å, b = 21.613(2) Å, c = 14.2066(13) Å, β = 99.789(5)°, and a volume of V = 7438.3(12) Å^3. It exhibits five-coordinate behavior, forming a slightly distorted pyramid with a square base. The paper also provides a detailed account of the crystal structures and reports spectroscopic study results. Electrochemical behavior is explored through cyclic voltammetry in CH_2Cl_2 as the solvent. Additionally, the reactivity of these compounds is predicted using various theoretical tools, such as Local and Global reactivity descriptors, Hirshfeld charge analyses, and Molecular Electrostatic Potential. To elucidate charge transfer processes, Time-Dependent Density Functional Theory is utilized. Various types of interactions are analyzed through the Quantum Theory of Atoms in Molecules and Non-Covalent Interaction analyses. Finally, conductivity is estimated using frontier molecular orbitals (FMO) and gap energies as crucial parameters.

Keywords: Radical ion salt, Hybrid-ligand complex, Cyclic voltammetry, Single-crystal X-ray, DFT, Charge transfer mechanism.

1. Introduction

In the realm of materials science, the study of hybrid-ligand complexes and mixed-valence radical ion salts stands as a pivotal endeavor, offering a gateway to unraveling intricate structural and electronic properties. They have exhibited many advantages such as reticular synthesis, ordered crystallinity, and porosity, as well as myriad functional applications, which have been expanded to gas adsorption [1],

separation [2], storage [3], delivery [4] of guest entities, single-site heterogeneous catalysis [5], and resistive sensing [6]. The development of these organic/inorganic compounds has attracted significant attention due to their potential for high-performance applications. Tetrathiafulvalene (TTF) and its derivatives are particularly promising due to their lower oxidation potential and excellent electron-donating abilities. These units can be reversibly oxidized to radical cation $TTF^{\bullet+}$ and dication TTF^{2+} [7]. Understanding the impact of charge transfer (CT) on the physical properties of redox-active MOFs; gives the chance for these redox-active materials to be used in the technological devices at the applied level. We mention the electrical switches [8], thermoelectric [9], fuel cells [10], super-capacitors [11], conductive and electrocatalysis [12], magnetic [13], and intelligent porous materials [14]. Thus, the combination of MOF structural diversity and the beneficial characteristics of organic/inorganic materials has enormous prospects for chemical and biological activities. Our primary objectives include thoroughly exploring the process of synthesis, revealing the detailed structure of crystals through single crystal X-ray analysis, and conducting a comprehensive theoretical investigation using Density Functional Theory (DFT). These compounds, made with ligands derived from the tetrathiafulvalene (TTF) donor molecule, show promise for novel applications in materials science. As we embark on this research journey, we aim not only to contribute significant insights into the design and properties of hybrid materials but also to pave the way for advancements in related disciplines. In the forthcoming sections, we delve into the intricate synthesis protocols, employing rigorous procedures such as solvent drying and distillation under an argon atmosphere to ensure precision. The resulting small, shiny black crystals were examined using scanning electron microscopy to confirm the success of the synthesis. Subsequent single crystal X-ray diffraction analysis overcomes challenges in data quality, revealing well-defined structures that offer insights into solvent-accessible voids and copper ion coordination, achieved through squeeze procedure. The electrochemical synthesis revealed the formation of the mixed-valence radical ion salt, $(Me_3TTF\text{-}CH{=}CH\text{-}Pyr)_2(PF_6)_3$, shedding light on the oxidation process. Further X-ray diffraction analysis of the resulting small black crystals unveiled the

distinctive structural features of the radical ion salt. Theoretical investigations, supported by DFT with the GGA-PBE functional, closely align with experimental data, providing a comprehensive understanding of geometrical parameters and charge transfer mechanisms. We also explored frontier molecular orbitals and conducted various computational analyses, including Hirshfeld atomic charges, QTAIM, molecular electrostatic potential maps, non-covalent interactions analysis, global/local reactivity descriptors, and bond energy decomposition analysis, to offer a holistic understanding of the stability, reactivity patterns, and bonding nature of these hybrid materials.

2. Materials and methods

2.1. Chemistry

The solvents have been dried and distilled according to the standard procedure; the experiment has been carried out under an argon atmosphere. IR spectra have been measured with a Bruker Equinox 55 spectrometer. The electronic spectrum has been recorded with a spectrophotometer UV-Vis Thermo-Scientific Evolution 220 model in CH_2Cl_2 solvent. The Cyclic voltammetry (CV) measurements have been carried out on the solution of $TBAPF_6$ 0.1 mmol. L^{-1} in CH_2Cl_2 with Ag/ AgCl as a reference electrode using a Potentiostat eDAQ instrument. Electrochemical analyses have been recorded at 100 mV/s with a platinum disk for the working electrode and platinum wire for the center electrode at room temperature. Melting points have been measured with a BÜCHI (B-545) Scientific melting point apparatus. Crystallographic data of black crystals have been collected at room temperature on an APEXII Bruker-AXS diffractometer equipped with graphite monochromated Mo–Kα radiation. The structures have been solved by direct methods with SIR-97 [15], which has revealed the non-hydrogen atoms of the molecules. Refinement has been performed by full-matrix least-square techniques based on F^2 with SHELXL [16] with the aid of the WINGX [17] program. All non-hydrogen atoms have been refined with anisotropic thermal parameters.

2.2.Chemical synthesis: Synthesis of the hybrid-ligand complex [Cu(hfac)$_2$(Me$_3$TTF-CH=CH-Pyr)].

The synthesis of the Me_3TTF-CH=CH-Pyr ligand has been reported by N. Benbellat et al. [18]. The present complex was synthesized as follows: (3 mg, 0.086 mmol) of Me_3TTF-CH=CH-Pyr dissolved in 90 ml of hot hexane are mixed with (20.54 mg, 0.043 mmol) of $Cu(hfac)_2$. xH_2O previously dissolved in 10 ml of hot hexane. Immediately, a purple solution is obtained, which is first cooled to room temperature and kept at 4°C for a few days. Small shiny black crystals are recovered and isolated by filtration. The scanning electron microscopy picture is shown in Figure 1. yielded 26 mg.

M.p: 262 °C, The selected IR data (KBr, υ/δ in cm^{-1}): 2920 υ(ArH), 1653-1607 υ(-C-O-), 1575 υ(C=C), 1563 υ(C=C), 1536 υ(C=C), 1502 υ(C=C), 1440-1390 υ(-C=N), 1261 υ(C-F), 1205, 1152-1104 υ(C–C), 1019 [In the plane δ(CH)], 937 δ(-C-O-), 703 υ(C–S), 667, 586 υ(Cu-N), 569, 527 υ(Cu-O).

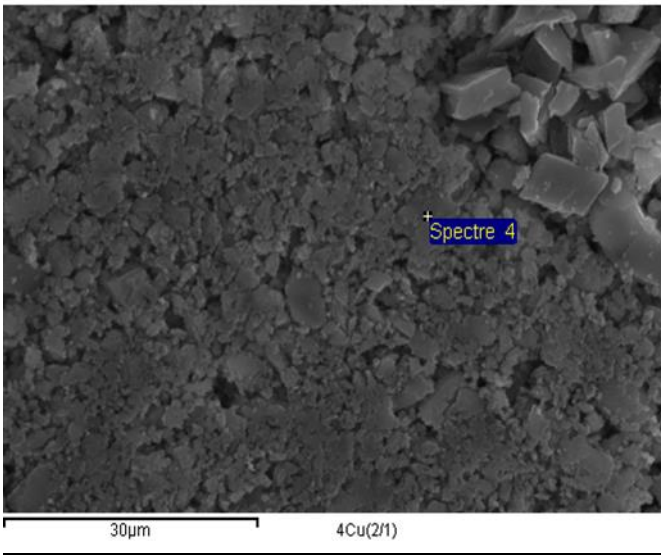

Figure 1: Scanning electron microscopy of the [$Cu(hfac)_2(Me_3TTF$-CH=CH-Pyr)] complex.

2.3.Electrochemical synthesis: synthesis of the mixed-valence radical ion salt (Me_3TTF-CH=CH-Pyr)$_2(PF_6)_3$

The electro-crystallization method consists, initially, of the oxidation of the organic donor D, which leads to the formation of the cation radical $D^{+\bullet}$. This latter is associated with the anionic species of the basic salt present in the solution to form the corresponding salt $D_m^{+}X_n^{-}$, which crystallizes or precipitates on the anode. The anion concentration should be much higher than that of the donor (about 20 times). Electro-

crystallization cells make it possible to obtain, in general, crystals of good quality. To limit the ligand diffusion, we carried out the electrochemical oxidation using a standard bridged U-shaped cell, containing a frit separating the anodic from the cathodic compartment. Both compartments are equipped with a platinum electrode 1 mm in diameter. Each compartment contains 80 mg of tetrabutylammonium hexafluorophosphate ($TBAPF_6$) as an electrolyte, 10 mg of (Me_3TTF-CH=CH-Pyr) donor are added to the anodic side and 10 ml of anhydrous CH_2Cl_2 are added to both compartments under an argon atmosphere. After the equilibrium of the solvent level at 4°C, the closed system is left under a current of 3 µA. After 15 days, small black crystals are deposited on the electrode (M.p: 241°C). X-ray analysis shows a radical ion salt structure $(Me_3$-CH=CH-TTF$)_2(PF_6)_3$.

2.4. X-ray diffraction analysis

2.4.1. Hybrid-ligand complex [Cu(hfac)$_2$(Me_3TTF-CH=CH-Pyr)].

Single crystal X-Ray diffraction data were collected at room temperature. The compound crystallizes in the monoclinic system, centrosymmetric space group C2/c with the following unit cell parameters a = 24.583(2) Å, b = 21.613(2) Å, c = 14.2066(13) Å, β= 99.789(5)°, V = 7438.8(12) $Å^3$. Table 1 collects the lattice parameters and the main refinement quality factors. Despite low-quality data, molecules are well-defined, and refinements revealed solvent-accessible voids of 284 $Å^3$ and numerous density peaks corresponding to very disordered hexane molecules. Then, the squeeze procedure was applied to the data. All atoms of the asymmetric unit are located in general positions. It contains one copper (II) ion lying in a five-members coordinated sphere of the nitrogen atom of the pyridyl ring of a Me_3TTF-CH=CH-Pyr (L) molecule and four oxygen atoms belonging to two hexafluoroacetylacetonate (hfac) ions (Figure 2). In such environment the complexes geometry can be characterized from the so-called tau value τ = (β–α)/60, with β and α the two largest angles around the central copper ion. τ is ranging from 0 for C_{4v} tetragonal pyramidal geometry to τ=1 for D_{3h} trigonal bipyramidal geometry [19–22]. According to this calculation, (α=162.4° and β=172.5° yielding τ=0.17 value), the copper ion has a square-based pyramid-like coordination sphere, in which the distorted square plane is formed by the N1 atom of the pyridyl ring, two

oxygen atoms O1, O2 of one hfac and the O4 atom of the second hfac, its second oxygen atom O3 being the axial atom (See Scheme 1).

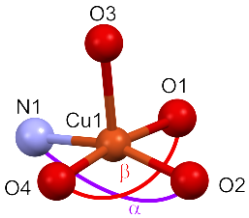

Scheme 1: Square-based pyramid-like coordination sphere of Cu^{II} ion showing the basal angles α and β in [Cu(hfac)$_2$(Me$_3$TTF-CH=CH-Pyr)] complex

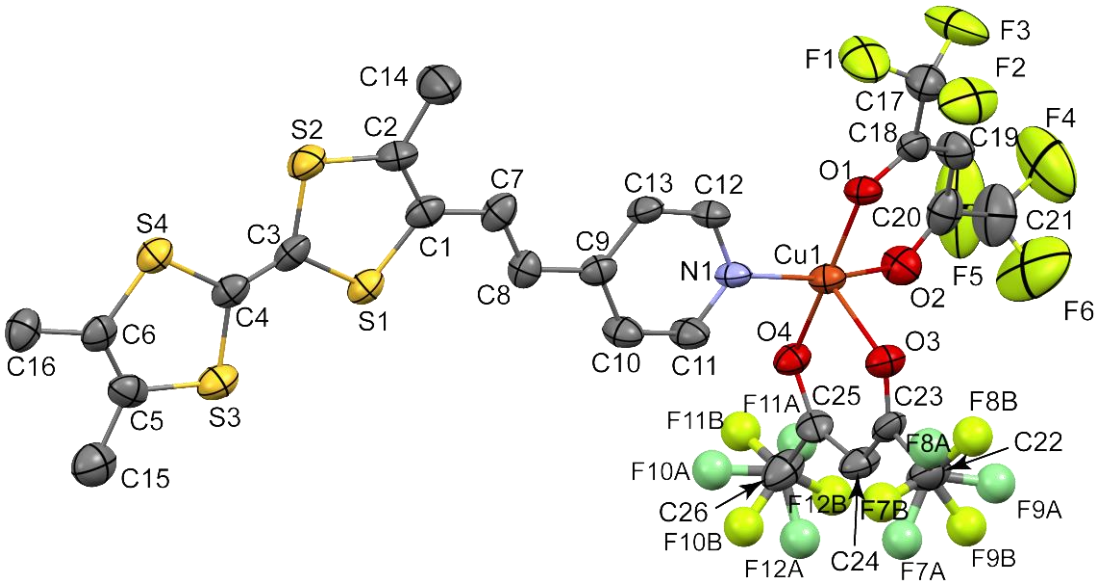

Figure 2: ORTEP (30%) view with labeling scheme of copper complex [Cu(hfac)$_2$(Me$_3$TTF-CH=CH-Pyr)]. Disordered fluoride atoms labeled A and B were drawn in ball and stick style for clarity.

In the equatorial plane, bond lengths involving copper ion are homogenous (see infra), with the apical distance Cu-O3 being 2.190(7) Å. The copper ion is expelled from the mean plane by 0.200(4) Å, as commonly observed in square-based pyramid-like coordination, this axial elongation is due to Jahn-Teller effect [23,24]. All angles at the apex of the copper, excluding those close to linearity (α and β used to calculate τ parameter) are between 84.0(3)° and 98.8(3)°. One can notice that in octahedral Cu(hfac)$_2$(L)$_2$ complexes, two different Cu-O lengths (ca. 2.0 and 2.2 Å) are usually found between an hfac anion and

the Cu^{II} ion [25]. In our compound, where copper is penta-coordinated, this characteristic is only found for the hfac anion which bears the apical atom O3 and the equatorial atom O4, (Cu-O4 length of 1.943(7)Å being the shortest equatorial distance) as observed in several compounds [26–29]. The oxygen atoms from the second hfac anion belong to the equatorial plane, they are coordinated to the copper by two homogeneous Cu-O1 and Cu-O2 short bonds of 1.949(7)Å and 1.960(8)Å respectively. The fourth equatorial atom N1 is bound to Cu(II) with 1.987(8) Å length.

A disorder is observed for the fluorine atoms of the two CF_3 groups of the hfac anion that bears O3 and O4. This fluorine disorder was treated with the SHELXL procedure SADI, in this constrained refinement C22 and C26 are the pivot atoms. Carbon C22 is bound to three fluorine atoms labeled F7A, F8A, F9A and three fluorine atoms labeled F7B, F8B, F9B, refinements give occupation factor of 0.58 for the group of atoms labeled A. The other pivot carbon C28 is bound to fluorine atoms labeled F10A, F11A, F12A and fluorine atoms labeled F10B, F11B, F12B, the occupation factor is 0.70 for atoms labeled A. Figure 3 shows the eight complexes contained in the mesh. The organic fragment Me_3TTF-CH=CH-Pyr is quite planar as the average plane of TTF and that of the pyridyl ring form an angle of 3.33(14)°. The pyridyl ring of the Me_3TTF-CH=CH-Pyr molecule forms an angle of 22.2(2)° with the square plane.

Table 1: Crystallographic data for $[Cu(hfac)_2(Me_3TTF\text{-}CH{=}CH\text{-}Pyr)]$

Empirical formula	$C_{26}H_{17}CuF_{12}NO_4S_4$
Deposition Number	2262291
Formula weight	827.18
Temperature, K	293(2)
Wavelength, Å	0.71073
Crystal system	Monoclinic
Space group	C2/c
a, Å	24.583(2)
b, Å	21.613(2)
c, Å	14.2066(13)
β, °	99.789(5)
Volume, $Å^3$	7438.3(12)
Z	8
Density (calculated), $g.cm^{-3}$	1.477
Absorption coefficient, mm^{-1}	0.902
F(000)	3304

Theta range for data collection	2.381 to 22.721°.
Index ranges	-26≤h≤18, -23≤k≤20, -15≤l≤11
Reflections collected	10235
Independent reflections	4825 [R(int) = 0.0636]
Completeness to theta = 22.721°	96.6 %
Refinement method	Full-matrix least-squares on F^2
Data / restraints / parameters	4825 / 60 / 489
Goodness-of-fit on F^2	0.972
Final R indices [I>2σ(I)] [a, b]	R_1 = 0.0774, wR_2 = 0.2260
R indices (all data) [a, b]	R_1 = 0.1478, wR_2 = 0.2774
Largest diff. peak and hole, e.Å^{-3}	1.105 and -0.402

[a] $R_1 = \Sigma||Fo| - |Fc|| / \Sigma|Fo|$. [b] $wR_2 = \{\Sigma[w (Fo^2 - Fc^2)^2] / \Sigma[w (Fo^2)^2]\}^{1/2}$.

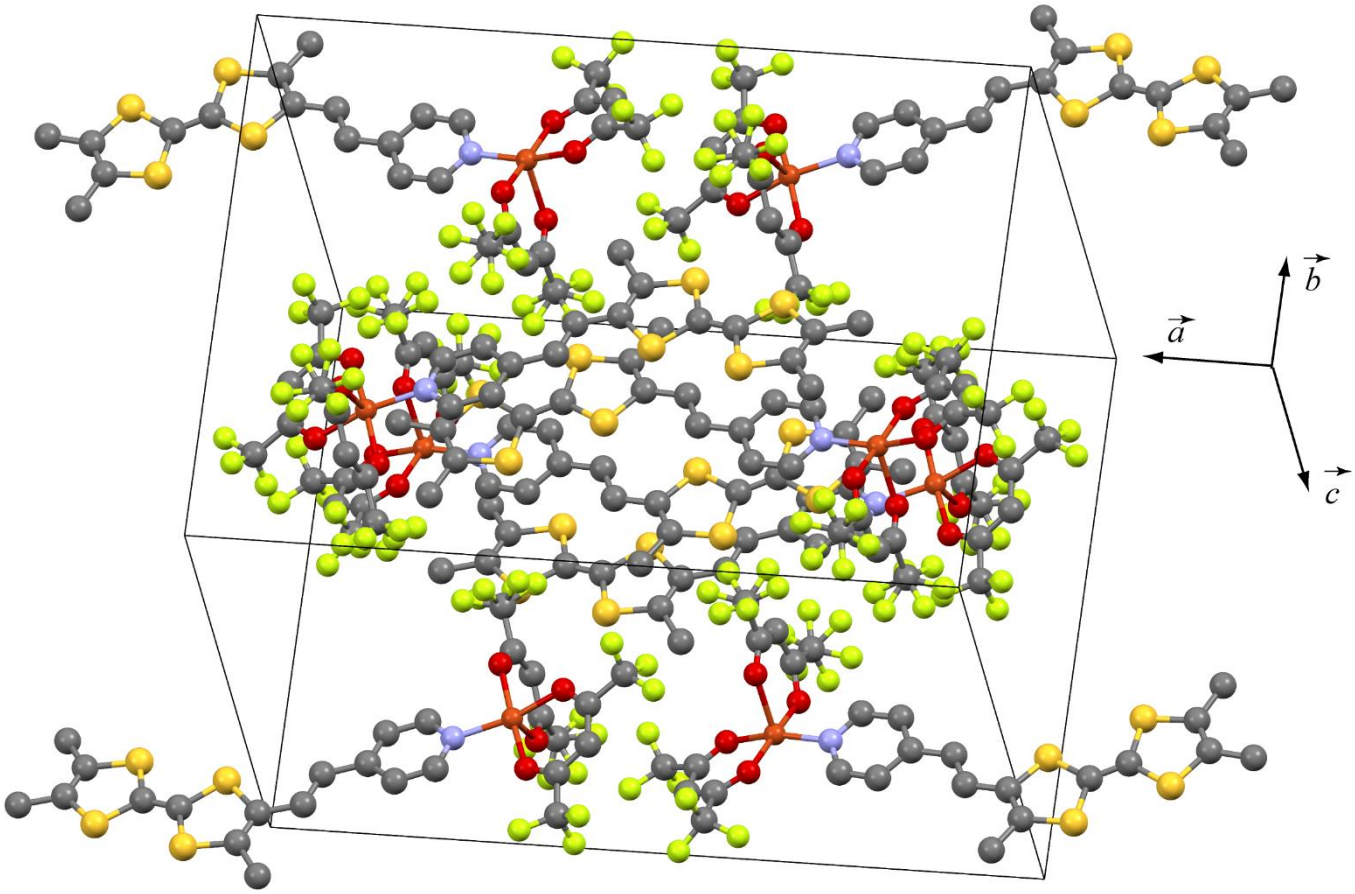

Figure 3: View of the eight complexes of [Cu(hfac)$_2$(Me$_3$TTF-CH=CH-Pyr)] in the centrosymmetric unit cell with copper ion in orange. Sulfur atoms from TTF fragment are drawn in yellow, oxygen in red, carbon in grey, nitrogen in blue. Only fluorine atoms labeled A from the two disordered CF_3 groups (labeled A and B) per complex were drawn in green.

There are no intermolecular contacts shorter than the corresponding van der Waals radii sum involving other atoms than hydrogen. Considering the complex in the asymmetric unit, the shortest intermolecular contacts are observed from each side of its TTF mean plane core (the four sulfur atoms and the two carbon atoms C3 and C4). One is observed between the hydrogen H15C of the pivot atom C15 from a methyl group and the oxygen O4 of the hfac anion ($d_{H15C\cdots O4}^{ii}$ = 2.569 Å with *ii* : -x, y, 1.5-z) from a complex, and another contact is observed between with S1 and $C7^{i}$, belonging to a complex packed on the other side of the TTF mean plane. This contact ($d_{S1\cdots C7}^{i}$ = 3.530(10) Å with *i* : -x, 2-y, 1-z) is larger than the corresponding van der Waals distance. These interactions lead to the stacking of head-to-tail molecules along the c-axis (see **Figure 4**). The shorter contact involving sulfur from asymmetric unit to the other side of the mean plane takes place from S1 to $C8^{ii}$, with a distance equal to 3.711(9)Å, a value larger the corresponding van der Waals radii.

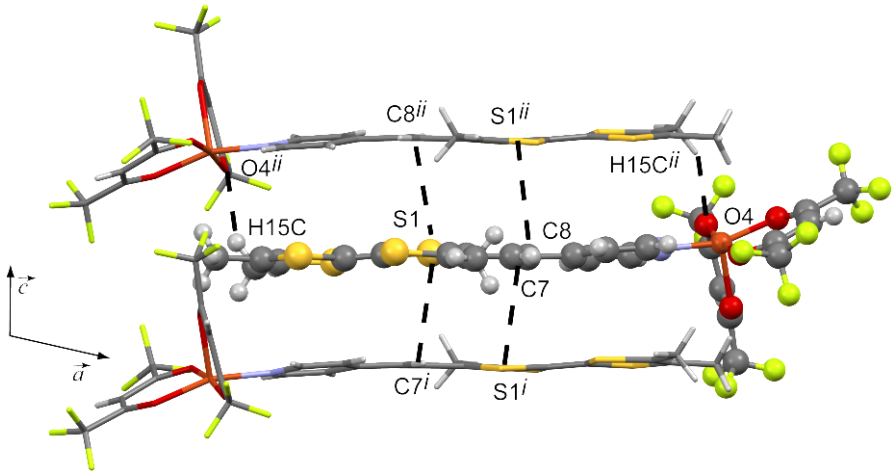

-a-

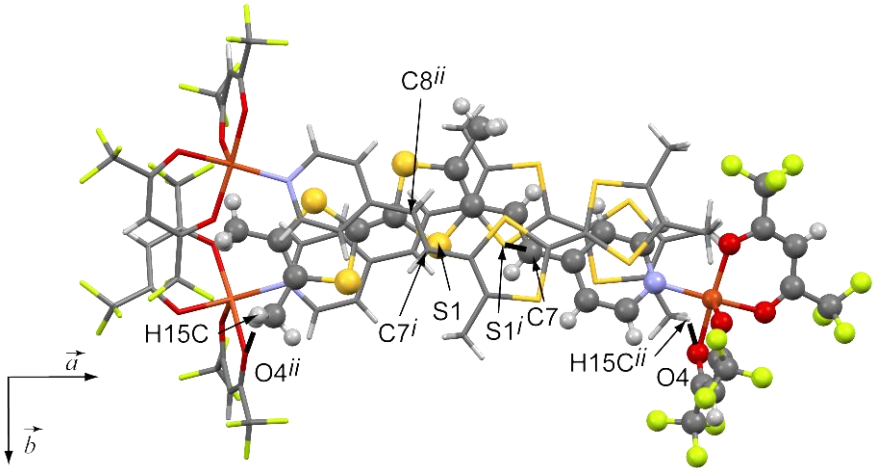

-b-

Figure 4: Short interactions between neighboring molecules [Cu(hfac)$_2$(Me$_3$TTF-CH=CH-Pyr)] along c axis view -a- in the *ac* place and -b- in the *ab* plane with the symmetries *i* : -x, 2-y, 1-z; *ii*: -x, y, 1.5-z for capped sticks molecules, ball and stick view molecule being the asymmetrical one. Only fluorine atoms labeled A are drawn.

Figure 5-a- represents the column of four complexes that are present in the mesh, two that appear to be strictly stacked without offset are represented in a "ball and stick" model, and the other two in a "wireframe". The same representations are used in the representation of Figure 5-b-, which shows the same molecules along with the crystallographic axis c. We can see more clearly that the complexes are not stacked by simple translation, but they are symmetrical concerning the sliding plane c. This view allows us to highlight the absence of contacts between the sulfur atoms of the TTF fragments skeletons.

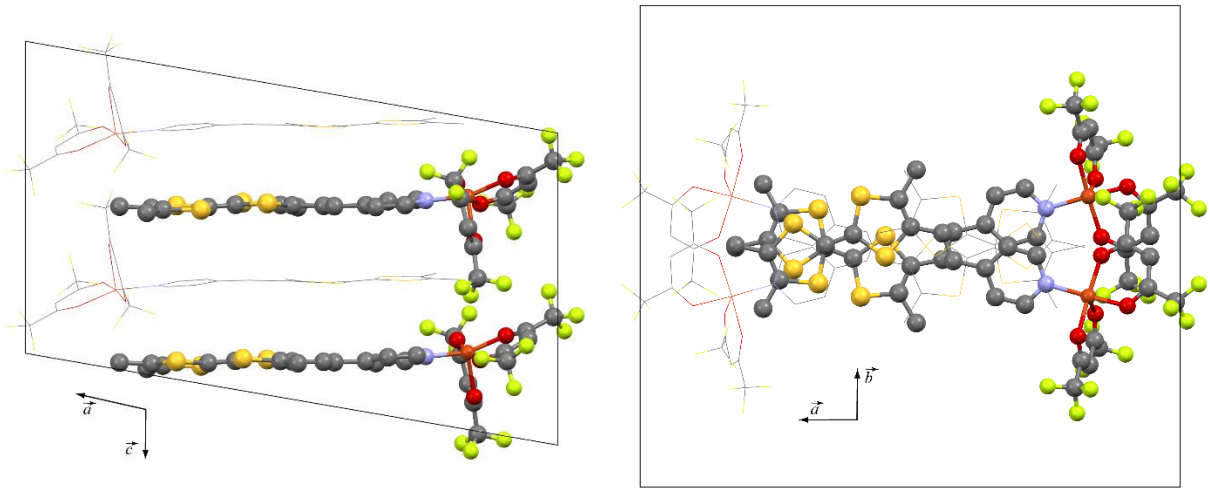

(a) (b)

Figure 5: Crystal structure of [Cu(hfac)$_2$(Me$_3$TTF-CH=CH-Pyr)]. Molecular packing depicted a) along the b-axis and b) along the *c*-axis.

The only short contacts smaller than the sum of the van der Waals radii found between complexes belonging to different "columns" are established from hydrogen H13 of the asymmetric complex to F12A^{iii}, this fluorine position being obtained from its symmetrical equivalent using the two-fold axis along b axis with x = 1/4 and z =3/4 (H13···F12A^{iii} = 2.614 Å with *iii* : ½-x, y-½, 1.5-z). From the same

asymmetric complex, two other contacts lightly greater than the sum of the van der Waals radii are found. The first one involving hydrogen from pyridyl ring H11 and F7A^{iv} (*iv* : ½-x, 2.5-y, 1-z) is 2.701 Å, this fluorine being the centrosymmetric equivalent of the asymmetric unit using inversion center in (¼ ,1.25, ½) position. The other one takes place from S2 and H24^{v}, this being symmetrical to the asymmetric unit thanks to C Bravais lattice (S2···H24^{v} = 3.043 Å with *v* : x- ½ , y – ½ , z). Asymmetric complex and complexes labeled *iii* and *v* are quite coplanar whereas complex labeled *iv* lies below this plane (see Figure 6).

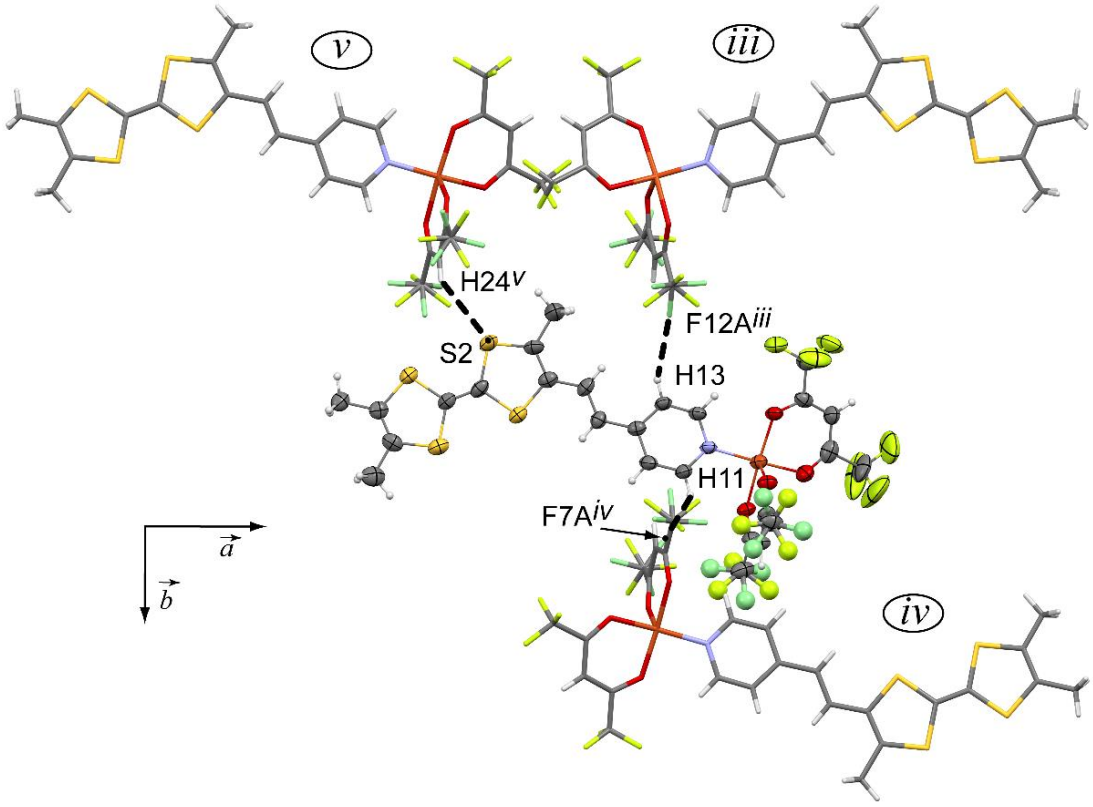

Figure 6: Short interactions between neighboring complexes [Cu(hfac)$_2$(Me$_3$TTF-CH=CH-Pyr)] viewed in the *ab* plane with symmetries *iii*: ½-x, y-½, 1.5-z ; *iv*: ½-x, 2.5-y, 1-z ; *v*: x- ½ , y – ½, z for capped sticks molecules representation, ORTEP view molecule being the asymmetrical one. Fluorine atoms labeled A are drawn in green, those labeled B are drawn in yellow-green color.

2.4.2. Mixed-valence radical ion salt (Me$_3$TTF-CH=CH-pyr)$_2$(PF$_6$)$_3$.

This compound crystallizes in the centrosymmetric triclinic Pī space group with cell parameters a=7.7015(7)Å, b=9.0815(10)Å, c=16.5171(14)Å, α=104.886(5)°, β=92.729(9)°, γ=101.140(4)°, and V=1089.64(18)Å^3; crystal data and the main refinements data are gathered in Table 2. The asymmetric unit cell contains one (Me_3TTF-CH=CH-Pyr) and one and a half PF_6^- anion, one in general position and the phosphorus P2 of one other lying on an inversion center (Figure 7).

Table 2: Crystallographic data for $(Me_3TTF\text{-}CH{=}CH\text{-}Pyr)_2(PF_6)_3$

Empirical formula	$C_{32}H_{30}F_{18}N_2P_3S_8$
Deposition Number	2262292
Formula weight	1133.97
Temperature	293(2) K
Wavelength, Å	0.71073
Crystal system	Triclinic
Space group	$P\bar{1}$
a, Å	7.7015(7)
b, Å	9.0815(10)
c, Å	16.5171(14)
α, °	104.886(5)
β, °	92.729(9)
γ, °	101.140(4)
Volume, Å^3	1089.64(18)
Z	1
Density (calculated), g.cm^{-3}	1.728
Absorption coefficient, mm^{-1}	0.628
F(000)	571
Theta range for data collection	4.445 to 25.542°.
Index ranges	-8≤h≤ 8, -10≤k≤h 10, -19≤l≤19
Reflections collected	5894
Independent reflections	3706 [R(int) = 0.0810]
Completeness to theta = 25.242°	92.5 %
Refinement method	Full-matrix least-squares on F^2
Data / restraints / parameters	3706 / 0 / 289
Goodness-of-fit on F2	1.157
Final R indices [I>2σ(I)] [a, b]	R_1 = 0.1322, wR_2 = 0.3249
R indices (all data) [a, b]	R_1 = 0.2144, wR_2 = 0.3830
Largest diff. peak and hole, e.Å^{-3}	1.385 and -0.561

[a] $R_1 = \Sigma||Fo| - |Fc|| / \Sigma|Fo|$. [b] $wR_2 = \{\Sigma[w (Fo^2 - Fc^2)^2] / \Sigma[w (Fo^2)^2]\}^{1/2}$.

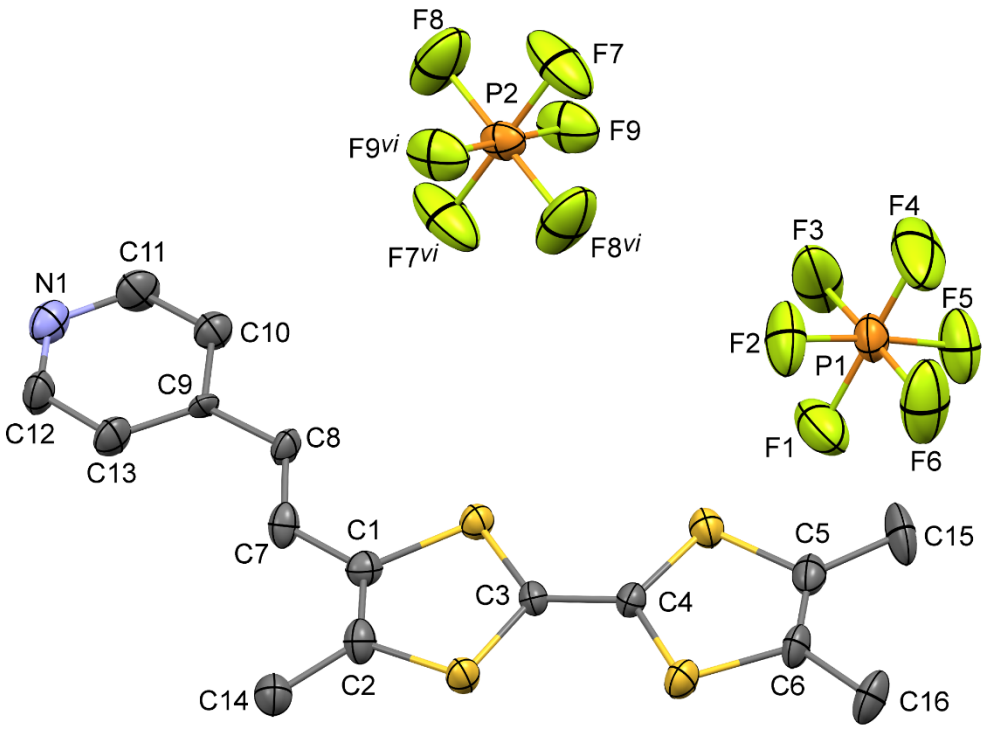

Figure 7: ORTEP view of compound $(Me_3TTF\text{-}CH{=}CH\text{-}Pyr)_2(PF_6)_3$ with 30% probability level showing the labelling scheme (symmetry code *vi*: -x, 1-y, 1-z).

The organic molecule is planar, considering the TTF core (the four sulfur atoms and the two carbon atoms C3 and C4) as a mean plane. The non-hydrogen atoms that are more out of the plane are C14, 0.211 Å below the plane, and C10, which is 0.146 Å above the plane. Figure 8-a shows TTF containing molecules packed along the *a*-axis to form organic columns. These columns alternate planes along the *b*-axis with parallel planes built of inorganic anions PF_6^-. (see Figure 8-b).

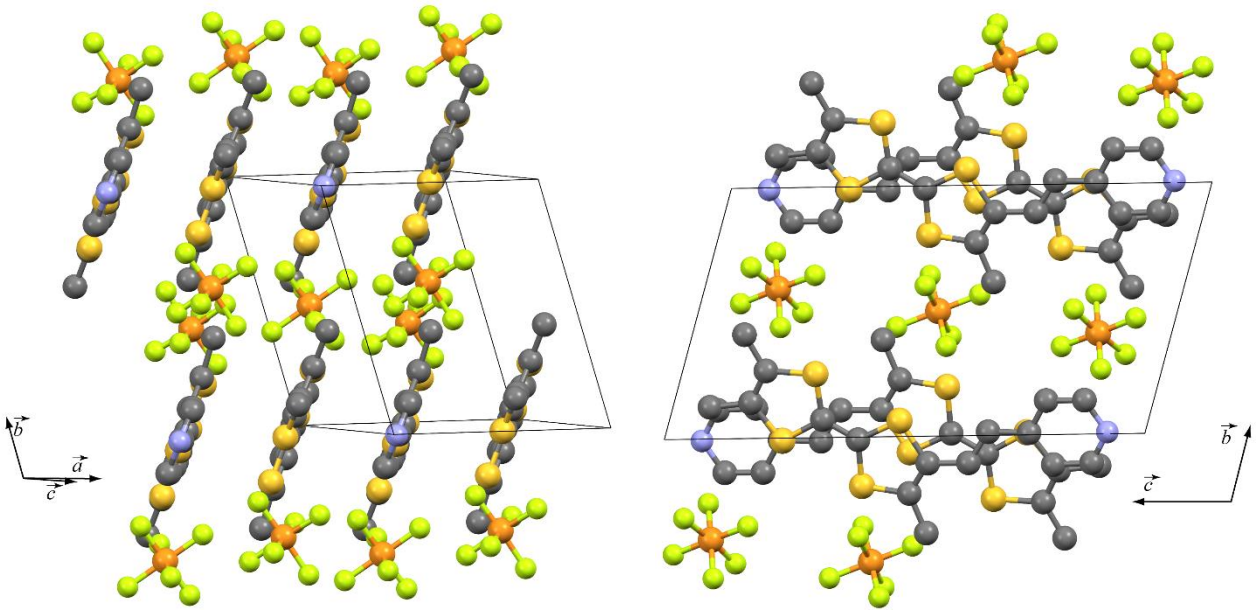

-a- -b-

Figure 8: Packing of compound $(Me_3TTF\text{-}CH{=}CH\text{-}Pyr)_2(PF_6)_3$ **-a-** view in the (101) plane; **-b-** view in the (100) plane.

The organic plane is built with Me_3TTF-CH=CH-Pyr which form columns. In the same column, neighboring TTF planes, on one side, are separated by 3.46 Å with the shortest intermolecular distance involving sulfur atoms S1···S1^{vii} equal to 3.712(6) Å (*vii*: 2-x, -y, 1-z) on the other side, TTF planes are separated by 3.39 Å with the corresponding distance S1···S2^{viii} equal to 3.489(5) Å (*viii*: 1-x, -y, 1-z). Also, the shortest interchain N1···N1^{ix} contacts (i*x* : 2-x, -y, -z,) were observed between Me_3TTF-CH=CH-Pyr units with contact lengths of 2.72(2) Å. In addition, a three-dimensional network is ensured by the anion through short interchain contacts (see Table 3). Thus, these contacts close to the van der Waals radii sum, were evaluated between fluorine atoms of PF_6^- in general position and seven adjacent Me_3TTF-CH=CH-Pyr units of two parallel columns. Several distances involved hydrogen atoms from Me_3TTF-CH=CH-Pyr, nevertheless two contacts bring into play non-hydrogen atoms, one between fluorine F3 and sulfur S4^{x} is 3.171(13)Å (*x*: x, 1+y, z), the other distance of 3.017(16)Å is observed in the asymmetric unit between F1 and C5. Short interactions are also observed between the three fluorine atoms of the PF_6^- lying into an inversion center, one of 3.052(8)Å takes place between F9 and S2^{ix},

whereas two other contacts shorter the van der Waals radii sum involved hydrogen atoms from Me_3TTF-CH=CH-Pyr. (See table 3).

Table 3 Short intermolecular contacts lower v-d-W radii for $(Me_3TTF\text{-}CH{=}CH\text{-}Pyr)_2(PF_6)_3$, in Å.

F1-C5	3.017(16)	F5-H16B^{xiii}	2.7292
F1-C15	3.177(19)	F5-H11^{xiv}	2.6382
F1-H15C	2.5557	F6-H15A^{xi}	2.7562
F1-H14C^{viii}	2.6850	F6-H16B^{xiii}	2.6117
F1-H13^{viii}	2.5090	F7-S2^{xv}	3.352(11)
F2-H15A^{xi}	2.7380	F7-H14A^{xv}	3.9937
F3-H14C^{viii}	2.7620	F7-H8^{xvi}	2.5977
F3-C14^{viii}	3.223(17)	F8-S1^{xvi}	3.290(14)
F3-S4^{x}	3.171(13)	F8-S3^{xvi}	3.323(11)
F4-H16A^{x}	2.7099	F9-H14A^{x}	2.7102
F5-H12^{xii}	2.5554	F9-S2^{x}	3.052(8)
F5-H15C	2.6697	F9-H14B^{viii}	2.6123

Symmetry codes : vii: 2-x,-y,1-z; *viii:* 1-x,-y,1-z; *ix:* 2-x,-y,-z; *x*: x,1+y,z; *xi:* x-1,y,z; *xii:* x,1+y,1+z; *xiii:* 1-x,1-y,2-z;*xiv:* 2-x,1-y,1-z*; xv:* x-1,y+1,z*; xvi:* 1-x,1-y,1-z.

2.5. Electrochemical properties

The redox behavior of the ligand (Me_3TTF-CH=CH-Pyr), the hybrid-ligand complex [$Cu(hfac)_2(Me_3TTF$-CH=CH-Pyr)], and the TTF as a reference were investigated by cyclic voltammetry. The measurements were performed using a working electrode (Pt), a reference electrode (Ag/AgCl), and $TBAPF_6$ (0.1 mol. L^{-1}) as the supporting electrolyte at a scan rate of 100mV/s. The cyclic voltammogram curves of these molecules are given in Figure 9. The oxidation potentials are listed in Table 4. According to the voltammograms, the copper ion is not concerned with the oxidation mechanism. The [$Cu(hfac)_2(Me_3TTF$-CH=CH-Pyr)] complex and the (Me_3TTF-CH=CH-Pyr) ligand displayed two separated reversible peaks, corresponding to the successive oxidation process of the TTF moiety from a neutral state to radical cation states, i.e., TTF^{+} and TTF^{++}. Their first oxidation potential was moved to

lower values than the TTF non-substituted (Table 4-a-), indicating that the modified TTF moiety in compounds is easier to be oxidized, this may be due to the donor effect of methyl groups. Contrarily, the dicationic states are more difficult to obtain in the modified TTF and their hybrid-ligand complexes than TTF non-substituted. The coordination effect is observed by comparing the potential oxidation of free moiety (Me_3TTF-CH=CH-Pyr) with the coordinated ones. To provide more information about the mechanism of oxidation, a comparative study was performed under the same conditions for [Cu(hfac)$_2$(Me_3TTF-CH=CH-Pyr)] complex.

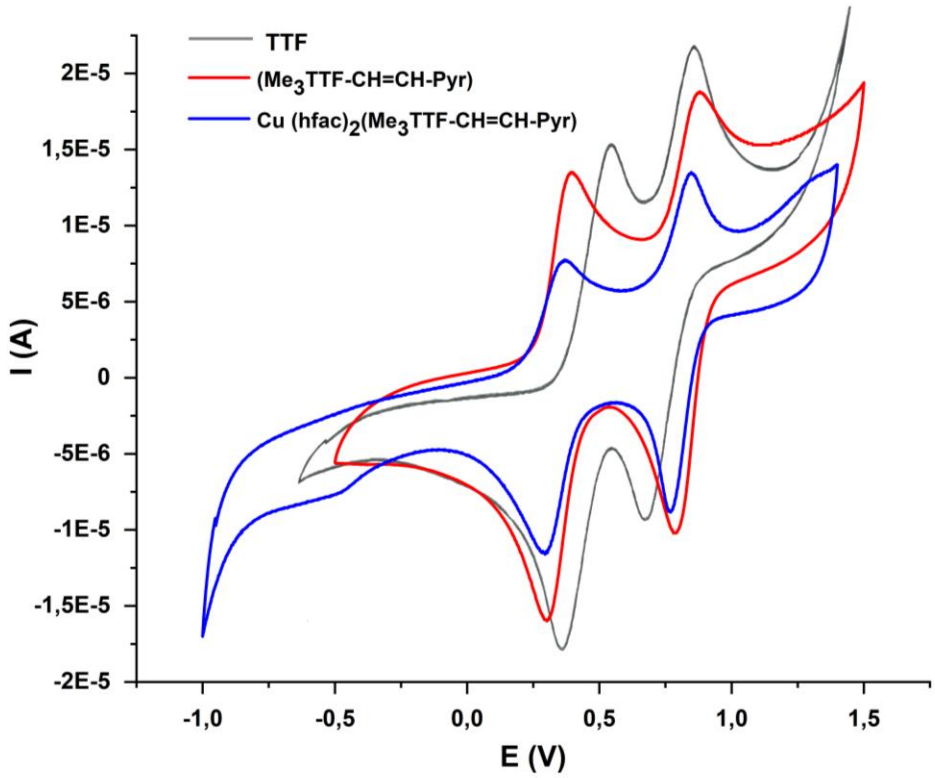

Figure 9: Cyclic voltammograms of the TTF (grey), (Me_3TTF-CH=CH-Pyr) ligand (red) and hybrid-ligand complex (blue), Rate = 100mV/S ; E_{ref}: Ag/AgCl ; E_{work}: Pt ; Solvent: CH_2Cl_2 ; Electrolyte: $TBAPF_6$ 0,1M.

Analyzing the results of cyclic voltammograms (Figure 9), the Copper complex exhibits two reversible oxidation potentials ($E_{ox1}^{1/2}$ = 0.34V, $E_{ox2}^{1/2}$ = 0.81V). The electrochemical process primarily occurs on the TTF moiety rather than the other moieties. The easier oxidation of the TTF unit in hybrid-ligand

complexes suggests a higher electron cloud density on this moiety due to the substituent effects. This is supported by the higher oxidation potential differences in the hybrid-ligand complex/TTF (Table 4-b-). The metal and substitution effects are observed by comparing the first and second oxidation potentials. The compounds (Me_3TTF-CH=CH-Pyr) and [Cu(hfac)$_2$(Me_3TTF-CH=CH-Pyr)] are slightly more easily oxidized than the TTF unit. Additionally, the Cu-N bonds reduce the electron-withdrawing effect of the hfac, causing the electron to return to TTF moiety.

Table 4-a-: Oxidation potentials of TTF unit, ligand, and mixed-ligand complex.

Molecules	$E_{ox1}^{1/2}$ (V)	$E_{ox2}^{1/2}$(V)
TTF	0.44	0.77
(Me_3TTF-CH=CH-Pyr)	0.35	0.84
[Cu(hfac)$_2$(Me_3TTF-CH=CH-Pyr)]	0.34	0.81

Table 4-b: Oxidation potentials difference of different systems; ligand/TTF, mixed-ligand complex/TTF, and mixed-ligand complex/ligand.

Molecules	$\Delta E_{ox1}^{1/2}$ (mV)	$\Delta E_{ox2}^{1/2}$ (mV)
(Me_3TTF-CH=CH-Pyr) / TTF	90	70
[Cu(hfac)$_2$(Me_3TTF-CH=CH-Pyr)] / TTF	100	40
[Cu(hfac)$_2$(Me_3TTF-CH=CH-Pyr)] / (Me_3TTF-CH=CH-Pyr)	10	30

3. Computational methods

All the calculations were performed using the AMS quantum chemistry package [30]. The Density Functional Theory (DFT) method was used with the generalized gradient approximation functional for change correlation energy, applying the PBE gradient-corrected exchange-correlation functional of Perdew-Burke-Ernzerhof [31] at the TZP (Triple Zeta Polarized) basis set [30]. Full geometries optimization of the ligand (Me_3TTF-CH=CH-Pyr) and the corresponding hybrid-ligand complex [Cu(hfac)$_2$(Me_3TTF-CH=CH-Pyr)] was carried out in the gas phase. The simulated UV-Visible

absorption spectra were obtained using the TD-DFT [32] method and the SAOP potential model [33]. Frequency calculations were performed to gather more information about the stability of these compounds. The Bond Dissociation Energy (BDE) was calculated using a fragment analysis preset to characterize the type of bonds at the coordination center. The Bond Critical Points (BCPs) are obtained at the level of QTAIM using the DGrid/Basin [34], and the Chem-Craft 1.4 [35] programs. Hirshfeld charges analysis, Molecular electrostatic potential (MEP) maps, Non-Covalent-Interactions (NCI) plot, and global and local chemical reactivity parameters were estimated through HOMO and LUMO energies and at the same level as the optimization.

4. Results and discussion

4.1. Molecular geometry of the complex

The optimized geometrical parameters of the ligand (Me_3TTF-CH=CH-Pyr) (Figure 10-a-) and the hybrid-ligand complex [Cu(hfac)$_2$(Me_3TTF-CH=CH-Pyr)] (Figure 10-b-) shown in Table 5, were calculated at different oxidation states by the DFT method with functional GGA-PBE at the TZP (Triple Zeta Polarized) basis set. Firstly, and as a general remark, all the obtained results of the geometrical calculations are in good agreement with the experimental data. The copper (II) ion is in a pyramid with a square base geometry. The square plane is formed by three oxygen atoms of the hfac ions and the nitrogen atom of the pyridyl ring. The calculated bond distances Cu-O(1), Cu-O(2), Cu-O(4), and Cu-N(1) are 1.930, 1.950, 1.935, and 1.946Å, respectively, which are slightly smaller than the experimental values 1.949(7), 1.960(8), 1.943(7) and 1.987(8)Å, respectively. The apical position is occupied by a fourth oxygen atom with Cu-O(3) calculated bond distance 2.111Å, it is slightly smaller than the experimental value 2.190(7)Å.

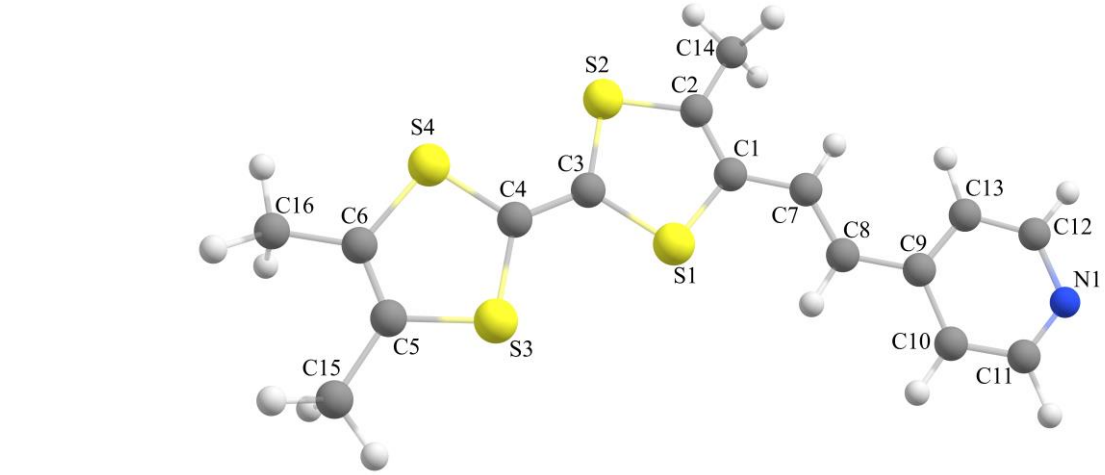

-a-

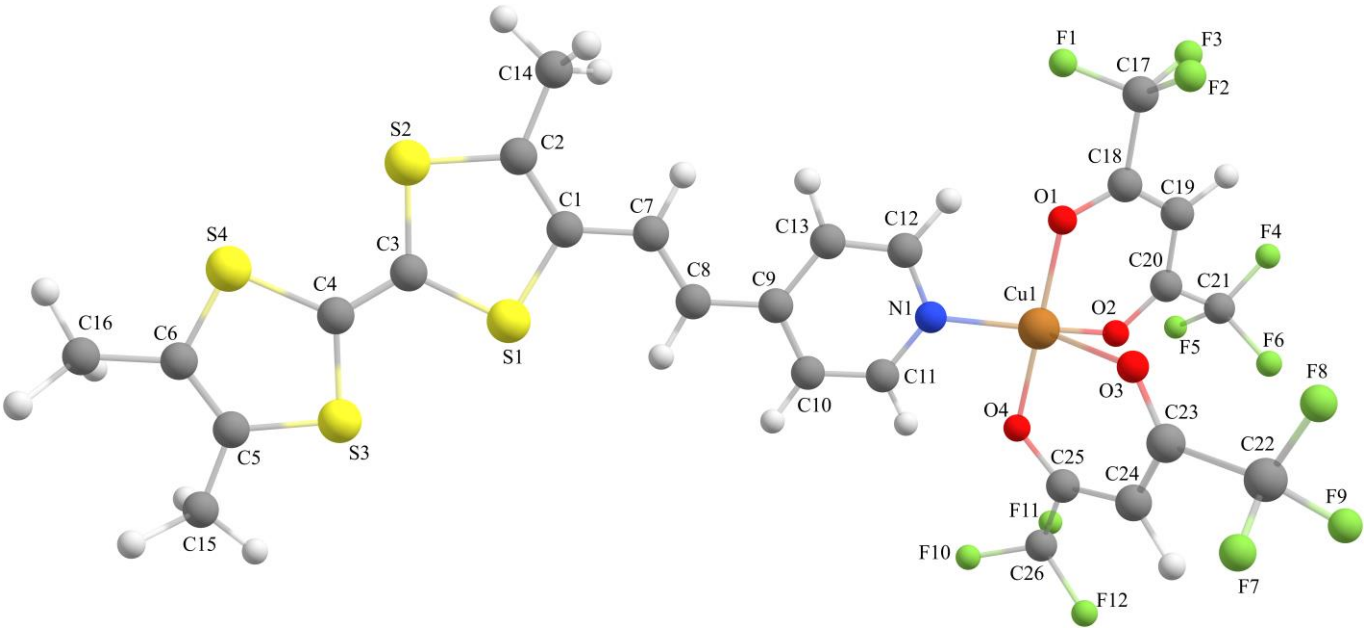

-b-

Figure 10: -a- The optimized structure of (Me_3TTF-CH=CH-Pyr) ligand [and -b- the optimized structure of Cu(hfac)$_2$(Me_3TTF-CH=CH-Pyr)] hybrid-ligand complex.

Table 5: Bond length, angles, and dihedral angles in (Me_3TTF-CH=CH-Pyr) ligand (L) and Cu(hfac)$_2$(L) complex.

	L^0		L^{1+}	$[Cu(hfac)_2(L)]^0$		$[Cu(hfac)_2(L)]^{1+}$	$[Cu(hfac)_2(L)]^{2+}$	$[Cu(hfac)_2(L)]^{3+}$	$[Cu(hfac)_2(L)]^{4+}$
	EXP	**PBE**	**PBE**	**EXP**	**PBE**	**PBE**	**PBE**	**PBE**	**PBE**
Bond length (Å)									
Cu1-O1	---	---	---	**1.949(7)**	1.930	1.987	1.835	1.893	1.834
Cu1-O2	---	---	---	**1.960(8)**	1.950	1.930	1.898	1.901	1.871

Cu1-O4	---	---	---	**1.943(7)**	1.935	1.895	1.832	1.907	1.844
Cu1-O3	---	---	---	**2.190(7)**	2.111	2.089	2.094	1.950	2.032
Cu1-N1	---	---	---	**1.987(8)**	1.946	1.978	1.949	1.971	1.960
N1-C12	1.324(16)	1.333	1.331	**1.351(11)**	1.341	1.339	1.338	1.338	1.339
N1-C11	1.368(18)	1.330	1.327	**1.321(12)**	1.339	1.335	1.335	1.336	1.337
C9-C8	1.460(13)	1.439	1.439	**1.482(13)**	1.432	1.438	1.440	1.443	1.443
C8=C7	1.337(16)	1.351	1.346	**1.331(14)**	1.351	1.346	1.346	1.347	1.352
C7-C1	1.451(14)	1.417	1.421	**1.447(14)**	1.412	1.419	1.422	1.424	1.425
C1=C2	1.414	1.359	1.368	**1.340**	1.360	1.365	1.370	1.381	1.387
C1-S1	1.760(11)	1.763	1.742	**1.749(11)**	1.757	1.742	1.735	1.726	1.726
C1-C2	1.488	1.484	1.476	**1.530**	1.483	1.478	1.477	1.474	1.472
C2-S2	1.710(11)	1.724	1.717	**1.722(12)**	1.713	1.713	1.708	1.700	1.698
S2-C3	1.709(11)	1.753	1.712	**1.759(12)**	1.733	1.718	1.709	1.697	1.701
S1-C3	1.711(11)	1.744	1.716	**1.758(10)**	1.744	1.722	1.711	1.701	1.699
C3=C4	1.407(13)	1.352	1.383	**1.334(14)**	1.354	1.378	1.395	1.414	1.419
C4-S3	1.694(11)	1.747	1.714	**1.754(11)**	1.736	1.718	1.708	1.696	1.698
C4-S4	1.700(11)	1.746	1.713	**1.739(10)**	1.738	1.721	1.709	1.696	1.701
S3-C5	1.752(12)	1.746	1.731	**1.748(13)**	1.740	1.723	1.715	1.705	1.697
S4-C6	1.700(11)	1.746	1.733	**1.737(12)**	1.738	1.726	1.714	1.703	1.696
C5=C6	1.363(18)	1.342	1.354	**1.334(15)**	1.341	1.353	1.364	1.377	1.393
C5-C15	1.479(18)	1.483	1.477	**1.480(16)**	1.481	1.478	1.475	1.470	1.464
C6-C7	1.470(16)	1.483	1.476	**1.490(14)**	1.481	1.476	1.475	1.470	1.464
Bond angles (°)									
O3-Cu-O1	---	---	---	**97.7(3)**	90.90	88.7	88.60	94.10	92.50
O3-Cu-O2	---	---	---	**98.8(3)**	93.90	92.8	92.50	93.20	88.80
O3-Cu-O4	---	---	---	**88.2(3)**	92.50	93.3	93.90	93.30	91.00
O3-Cu-N1	---	---	---	**98.4(3)**	109.30	110.5	109.50	107.20	111.30
O4-Cu-N1	---	---	---	**92.9(3)**	91.10	90.50	89.50	90.60	90.00
O4-Cu-O2	---	---	---	**84.0(3)**	84.50	85.00	85.30	85.30	85.80
O2-Cu-O1	---	---	---	**90.5(3)**	92.40	93.50	94.60	91.30	93.20
O1-Cu-N1	---	---	---	**90.7(3)**	90.50	90.00	89.60	90.00	89.60
O4-Cu-O1	---	---	---	**172.5(3)**	175.50	177.50	177.5	171.90	176.30
O2-Cu-N1	---	---	---	**162.4(3)**	156.60	156.60	157.70	159.40	159.6
Dihedral angles									
C8=C7-C1-S1	-4.3	4.3	360.0	**-3.1**	4.60	5.70	5.50	6.30	7.40
C2-S2-C3-S1	3.4	7.8	0.5	**-7.0**	4.90	2.70	359.90	0.50	359.70
C1-C7=C8-C10	171. 8	175.1	181.0	**-180.0**	174.60	173.20	171.50	169.80	171.90
C13-C9-C8=C7	10.1	6.0	359.0	**-5.6**	6.50	6.40	8.80	8.00	8.90

Where: L^0 neutral Ligand, L^{1+}: oxidized ligand.

When the oxidation state is increased, there is a slight decrease in Cu-O bond length values, while the Cu-N bond length value became slightly larger. Additionally, all the O-Cu-O angle bonds of the pyramidal geometry are close to 90°, while the O(3)-Cu-N(1) angle is slightly wider than 90°. In the exception, the calculated O(4)-Cu-O(1) and O(2)-Cu-N(1) angles of the square base are 175.50° and 156.60°, respectively, which are slightly different from the experimental values of 172.5(3) and 162.4(3)°, respectively. In the coordinated (Me_3TTF-CH=CH-Pyr) unit, the bond distances are slightly larger than in the free state. They are unchanged when increasing the oxidation degree, except for C(1)-

S(1), C(23)-S(2), C(3)-S(2), C(3)-S(1), C(4)-S(3), C(4)-S(4), C(5)-S(3) and C(6)-S(4) bond distances, which decrease slightly. The electron removal is located in the ylidene region, which results in π-π stacking in the crystal structure, confirmed by the C4=C3 distance values (Table 5). Furthermore, the dihedral angles C(8)=C(7)-C(1)-S(1), C(1)-C(7)=C(8)-C(10), C(13)-C(9)-C(8)=C(7), and C(2)-S(2)-C(3)-S(1) with the values 4.60°, 174.60°, 6.50°, and 4.904°, respectively, do not allow the Me_3TTF-CH=CH-Pyr molecule to be rigorously planar. There is no change in the dihedral angle values when increasing the oxidation degree.

4.2. Frontier Molecular Orbitals analysis

The HOMO and LUMO frontier molecular orbitals play significant roles in the description of reactivity and kinetic stability, and intramolecular charge transfer (ICT) in molecules. The view of the presentation of the principal molecular orbitals (Figure 11) shows that the HOMO of the free ligand at the neutral and the first oxidation states with alpha spin are distributed throughout the entire TTF side ($2p_z$ orbitals), while the LUMO is located on the 4-vinyl pyridine. On the other hand, at beta spin, the HOMO was mainly centered on the nitrogen-px and nitrogen-2s orbitals, while the LUMO is on the TTF side. After coordination, a donor-acceptor charge transfer mechanism is observed at different oxidation states. The electron clouds of the HOMO orbital are mainly distributed on the TTF moiety due to its stronger electron donor properties. However, the LUMO orbital is located on the metal ion. Specifically, the $d_{x^2-y^2}$ and d_{xy} orbitals indicate how electron delocalization can involve the entire system. Additionally, the frontier orbitals of the optimized structures at different oxidation states translate the charge transfer. The HOMO orbital at the first oxidized state is localized on the Cu-$d_{x^2-y^2}$ orbital, while in the dicationic state, it occupies a wider area and is located mostly on the Cu-$d_{x^2-y^2}$, Cu-d_{xy}, Cu-d_{xz}, Cu-d_{z^2}, and O-pz orbitals. In the dicationic state, the LUMO orbital is located on the TTF core. This description is also applicable to the 3+ oxidation state. However, the HOMO of the complex at 4+ oxidized state is centered

on the 4-vinyl pyridine side, while, the LUMO is observed around the Cu-$d_{x^2-y^2}$, and O-py orbitals. The results of Table 6 show that the calculated gap energy separating the Highest occupied molecular orbital from the lowest unoccupied molecular orbital for $[Cu(hfac)_2(L)]^0$, $[Cu(hfac)_2(L)]^{1+}$, $[Cu(hfac)_2(L)]^{2+}$, $[Cu(hfac)_2(L)]^{3+}$, and $[Cu(hfac)_2(L)]^{4+}$ hybrid-ligand complexes at alpha spin are 1.014, 1.15, 0.018, 0.019 and 0.624 eV, respectively. While, at beta spin, they are equal to 0.061, 0.102, 0.671, 0.228, and 0.035 eV, respectively. The lower bandgap exists in $[Cu(hfac)_2\ (L)]^{2+}$ and $[Cu(hfac)_2\ (L)]^{3+}$ complexes with alpha spin, revealing the highest conductivity character of the resulting materials.

Table 6: Calculated energies in (eV) of molecular orbitals of the ligand, neutral, and oxidized complex at the GGA-PBE level.

	α-spin									**Energy (eV)**
	H-3	**H-2**	**H-1**	**S**	**L**	**L+1**	**L+2**	**L+3**	**Gap**	
$[Cu(hfac)_2(L)]^0$	-6.003	-5.725	-5.253	-4.560	-3.546	-3.448	-3.080	-2.817	1.014	-388.816
$[Cu(hfac)_2(L)]^{1+}$	-8.221	-8.021	-7.828	-7.482	-6.332	-5.977	-5.417	-5.172	1.15	-382.600
$[Cu(hfac)_2(L)]^{2+}$	-11.498	-11.005	-10.832	-10.278	-10.260	-8.839	-8.375	-8.281	0.018	-373.629
$[Cu(hfac)_2(L)]^{3+}$	-14.093	-13.767	-13.611	-13.023	-13.004	-11.449	-11.105	-10.629	0.019	-361.776
$[Cu(hfac)_2(L)]^{4+}$	-17.059	-16.715	-16.614	-16.505	-15.881	-15.155	-13.880	-13.478	0.624	-347.170
	H-3	**H-2**	**H-1**	**H**	**L**	**L+1**	**L+2**	**L+3**	**Gap**	
L^0	-6.334	-5.847	-5.584	-4.188	-2.910	-2.255	-1.486	-1.290	1.278	
	β-spin									
	H-3	**H-2**	**H-1**	**H**	**L**	**L+1**	**L+2**	**L+3**	**Gap**	
$[Cu(hfac)_2(L)]^0$	-6.020	-5.924	-5.501	-4.547	-4.486	-3.527	-3.401	-3.055	0.061	-388.816
$[Cu(hfac)_2(L)]^{1+}$	-8.927	-8.569	-8.098	-7.731	-7.629	-6.700	-3.401	-3.055	0.102	-382.600
$[Cu(hfac)_2(L)]^{2+}$	-11.619	-11.444	-10.984	-10.784	-10.113	-10.084	-6.267	-5.920	0.671	-373.629
$[Cu(hfac)_2(L)]^{3+}$	-14.506	-14.195	-13.866	-13.466	-13.238	-12.978	-8.801	-8.327	0.228	-361.776
$[Cu(hfac)_2(L)]^{4+}$	-17.287	-16.967	-16.522	-16.487	-15.881	-16.376	-12.335	-11.429	0.035	-347.170
L^0	-6.334	-5.847	-5.574	-4.188	-2.910	-2.255	-1.486	1.290	1.278	

Where H: HOMO, S: SOMO, L: LUMO, L in the formula is neutral Ligand Me_3TTF-CH=CH-Pyr.

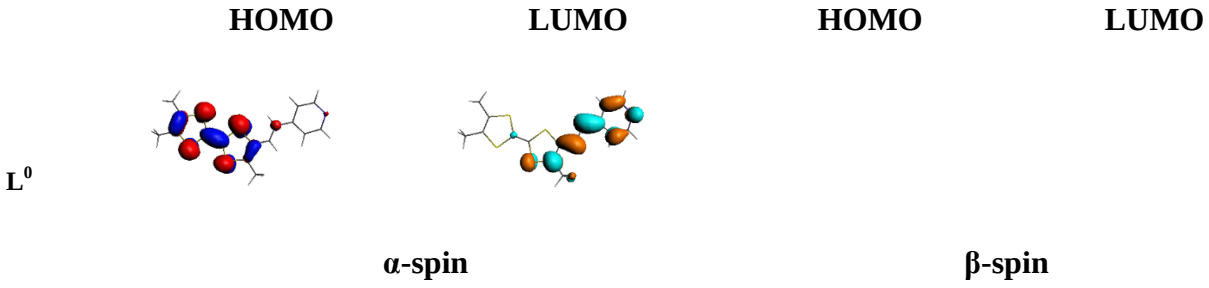

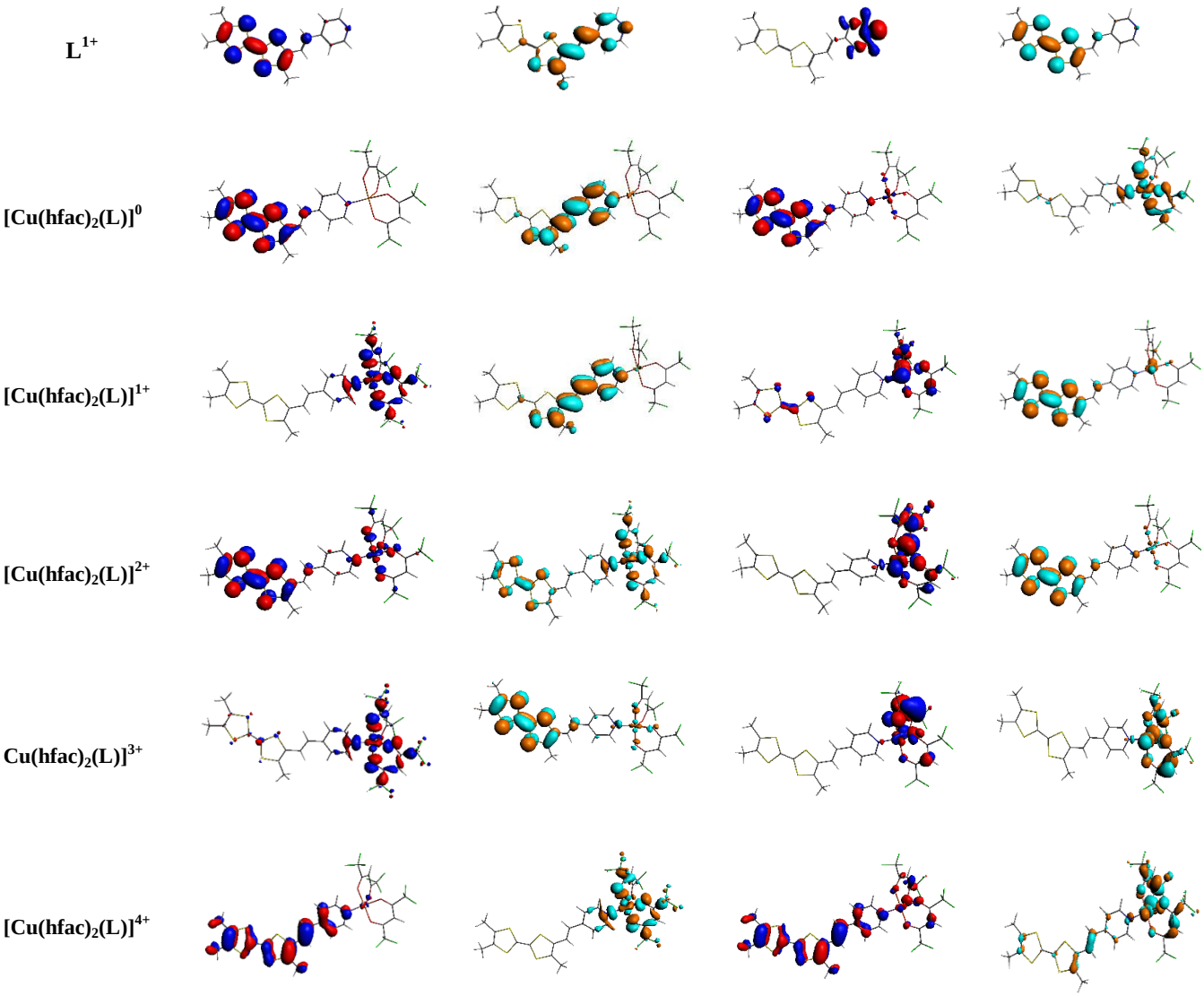

Figure 11: Molecular orbital distribution of frontier HOMOs and LUMOs for the ligand and the complex at different oxidation states.

4.3. Hirshfeld Atomic Charges (HAC)

The Hirshfeld atomic charges (HAC) of the (Me_3TTF-CH=CH-Pyr) and the corresponding [Cu(hfac)$_2$(Me_3TTF-CH=CH-Pyr)] hybrid-ligand complex at different oxidation states were calculated at the same level of theory as the optimization and the summary of the findings were provided in Table 7. The Hirshfeld charges [36] are defined relative to the deformation density, which represents the difference between the molecular and unrelaxed atomic charge densities. These charges are significant in the study of molecular systems as they can help explain chemical reactivities, dipole moments, and

polarizabilities of a molecular structure. An atomic charge analysis of the hybrid-ligand complex reveals that that the copper (II) ion is the most positively charged (0.400 e-), and this charge increases with the degree of oxidation, making it a possible location for the electron removal. Conversely, the O(4) atom is the most negatively charged (-0.202 e-). Briefly, most carbon atoms are negatively charged, except for C(12), C(11), and C(9), which carry positive charges of 0.018 e^-, 0.015 e^-, and 0.020 e^-, respectively. This is due to their positions in the aromatic cycle towards the nitrogen atom. The ligand-metal donation effect is confirmed by the positive atomic charge of the Cu and the negative atomic charge of the nitrogen pyridine atom. Additionally, after the complexation of the (Me_3TTF-CH=CH-Pyr) unit, the positive charges located on the sulfur atoms increase, while the negative charges located on the carbon atoms of the TTF unit decrease. The same variation in the mode of the HAC was observed when increasing the oxidation degree.

Table 7: Hirshfeld atomic charge of the ligand and the hybrid-ligand complex calculated with the GGA-PBE method at different degrees of oxidation.

Atom	L^0	L^{1+}	$[Cu(hfac)_2(L)]^0$	$[Cu(hfac)_2(L)]^{1+}$	$[Cu(hfac)_2(L)]^{2+}$	$[Cu(hfac)_2(L)]^{3+}$	$[Cu(hfac)_2(L)]^{4+}$
C1	-0.042	-0.018	-0.043	-0.028	-0.016	0.003	0.008
C2	-0.022	-0.003	-0.017	-0.003	0.011	0.027	0.041
C3	-0.100	-0.006	-0.100	-0.073	-0.054	-0.034	-0.019
C4	-0.093	-0.064	-0.092	-0.071	-0.057	-0.042	-0.038
S1	0.068	0.176	0.082	0.156	0.205	0.263	0.284
S2	0.088	0.190	0.115	0.179	0.233	0.297	0.326
S3	0.069	0.181	0.089	0.168	0.225	0.288	0.318
S4	0.064	0.180	0.084	0.169	0.231	0.296	0.329
N	-0.167	-0.135	-0.091	-0.076	-0.063	-0.068	-0.051
C11	0.000	0.020	0.018	0.029	0.039	0.044	0.053
C12	0.000	0.019	0.015	0.027	0.036	0.043	0.049
C10	0.050	-0.035	-0.040	-0.027	-0.016	-0.006	0.008
C9	0.012	0.013	0.020	0.025	0.034	-0.038	0.052
C8	-0.057	-0.023	-0.057	-0.035	-0.023	-0.001	0.008
C7	-0.059	-0.054	-0.056	-0.047	-0.028	-0.032	-0.014
Cu	/	/	0.400	0.427	0.465	0.503	0.521
O1	/	/	-0.169	-0.158	-0.137	-0.141	-0.110
O2	/	/	-0.177	-0.162	-0.139	0.129	-0.103
O3	/	/	-0.183	-0.170	-0.145	-0.145	-0.113
O4	/	/	-0.202	-0.194	-0.182	-0.124	-0.102

Where: L: Me_3TTF-CH=CH-Pyr.

4.4. Topological QTAIM analysis

We conducted a topological analysis of the electron density using the QTAIM approach and supported by the Dgrid-4.6 program, [34]. Our goal was to understand the nature of the chemical and physical bonding and to explore the different interactions in the studied systems, including covalent and non-covalent interactions. Specifically, we focused on investigating the ligand-ligand and ligand-PF_6 counter ions interactions. Single point density-functional theory (DFT) calculation is used to investigate the topological parameters (electron density ρ (r), Laplacian of the density $\nabla^2\rho(r)$, V(r) / G(r) ratio, total electronic energy H(r), and the ellipticity values (ε)) of the present hybrid-ligand complex and the radical ion salt in various arrangements. These parameters are documented in the supporting information, and bond lengths and critical points are depicted in Figure 12. The white balls represent the atom critical points (ACP), the interactions between these atoms are identified by bond critical points BCP (in red), the formation of cycles and cages are characterized by ring critical points RCP (in green) and cage critical points CCP (in blue), respectively [37–39].

At the level of the hybrid-ligand complex, the topological parameters are used in the investigation of the coordination mode of donor units (Me_3TTF-CH=CH-Pyr) to a copper center $Cu(hfac)_2$. The existence of a connection between these two is indicated by the presence of a critical point. The QTAIM results of the neutral hybrid-ligand complex show that all the values of BCP density at the M-ligand (Cu-N and Cu-O) bonds are higher than 0.1 and less than 1.0, with relatively high positive Laplacian values $\nabla^2\rho(r)$ indicating a closed shell interaction. The degree of covalency of a given interaction is reflected by the magnitude of HBCP. The partially covalent character is observed for all the states and is conditioned by $\nabla^2\rho_{BCP} > 0$ and $H_{BCP} < 0$, indicating a medium strength. In the oxidized states, the density values at the same BCPs are less than or equal to 0.1. These values, along with relatively small and positive Laplacian values $\nabla^2\rho(r)$ indicate a mainly non-covalent interaction, specifically a closed shell interaction [40,41]. The larger Value of ρ(BCP) found in the Cu-N bond estimates the strength of this bond, even though it is remarkably longer than some of the Cu-O-bonds (larger than Cu-O1 and Cu-O4 at the neutral state and larger than Cu-O2 in the first oxidized state). This indicates that the strength of the interactions is

opposite to the trend in these bond lengths. In the $[Cu(hfac)_2(L)]^{2+}$, $[Cu(hfac)_2(L)]^{3+}$ and $[Cu(hfac)_2(L)]^{4+}$ hybrid-ligand complexes, the interactions between copper (Cu) and oxygen (O) are slightly stronger than the interactions between Cu and nitrogen (N), except for the Cu-O4 bond. Specifically, in the $[Cu(hfac)_2(L)]^{2+}$, the strength of interactions is ranked as follows: Cu-O3 > Cu-O1 > Cu-N > Cu-O2 > Cu-O4, based on the electron density at the bond critical point (ρBCP). For the $[Cu(hfac)_2(L)]^{3+}$, the ranking is Cu-O1 > Cu-O2 > Cu-O3 and Cu-N > Cu-O4. In the $[Cu(hfac)_2(L)]^{4+}$ complex, the ranking is Cu-O1 > Cu-O3 > Cu-O2 and Cu-N > Cu-O4. These results can be explained by the mesomeric effect in hfac parts. The compound shows intramolecular interactions, specifically the C-H···O interactions. From Figure 12-a-, the most significant connections are N-C12-H12···O1-C (approximately 2.053 Å) and N-C11-H11···O4-C (approximately 2.065 Å). These two critical points are characterized by a low positive value of ρ(r). It is observed that the electronic density at the level of these two points increases remarkably when transitioning from the neutral to the first oxidized state (0.34 to 0.023 a.u.). Additionally, the H(r) values increase with the increase in oxidation degree. According to Espinosa et al. [42], these interactions can be estimated as weak hydrogen bonds. The present structure exhibits additional H·····H interactions, located between C8=C7-H7 and H13-C13 due to the formation of the six-center cycle, which is apparently absent in the complexes with the formal charge 4+. The absence of the RCP around C_4H_2 at the same state is observed due to the change in geometry caused by the di-oxidation of the copper (Table 7), specifically the change in the dihedral angles. Moreover, two five-center cycles are found, namely $CuONC_{12}H_{12}$ and $CuO_3NC_{11}H_{11}$. From the QTAIM results, the polarity of the cycles is in the order CuNCHO > CuO_2C_3 > C_5N > C_3S_2. This may be explained by the ellipticity values which give the degree of π-character. The C_4H_2 ellipticity values increase with the oxidation degree from zero to 2+, reaching 6.96, 7.81, and 15.87 at the dicationic state, and becoming 2,68 at the 3+ state. This is supported by the argument that the Ring CP formed at the level of the C_4H_2 atoms group is getting closer to the BCP related between H7 and H13.

The superposition of the corresponding RCP and BCP is noted at the 3+ oxidized state (Figure 12-a, 12-b, 12-c, and 12-d).

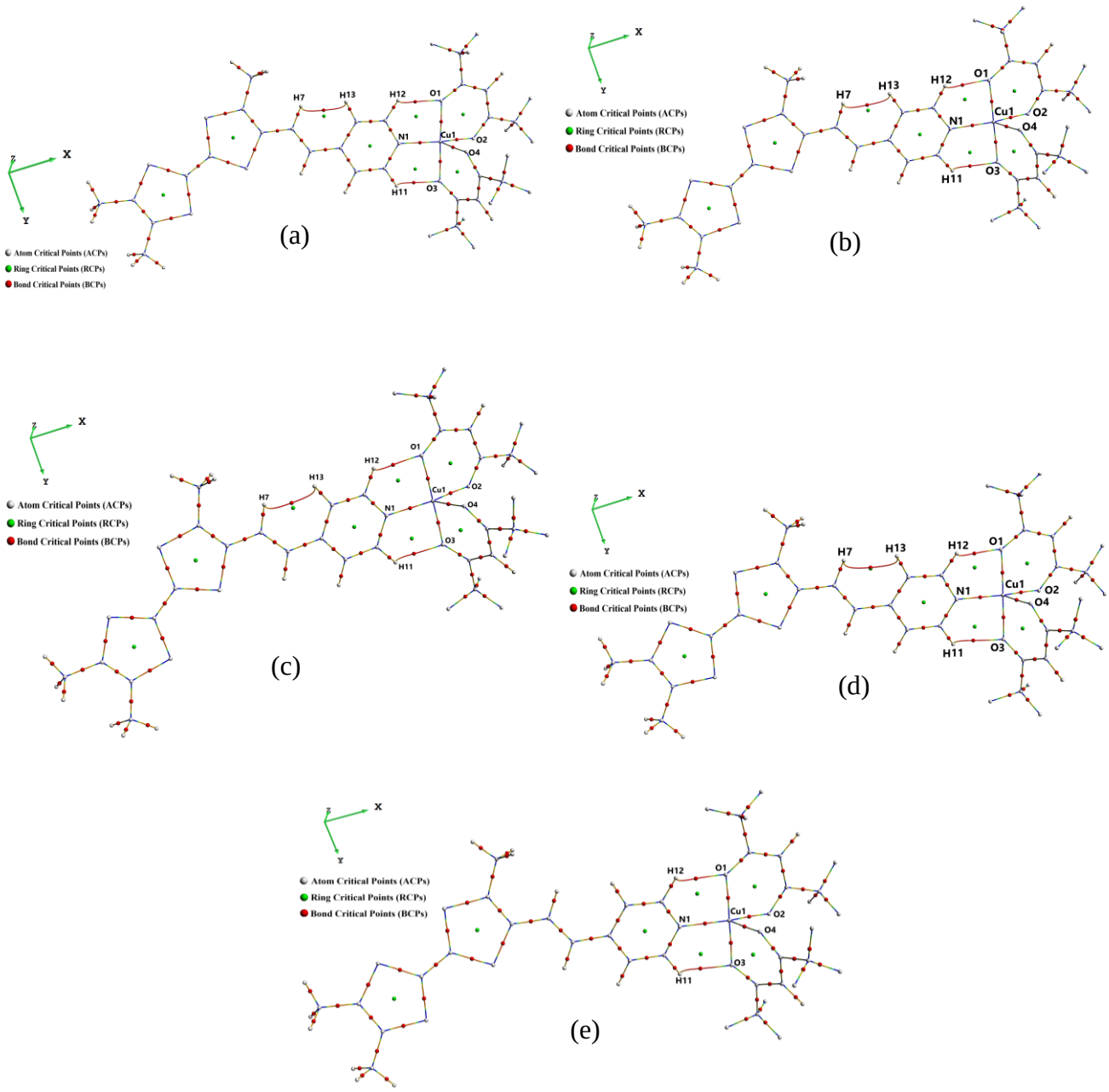

Figure 12: Molecular graph of the neutral (a) and oxidized (1+ (b), 2+ (c), 3+ (d), 4+ (e)) states of [Cu(hfac)$_2$(Me$_3$TTF-CH=CH-Pyr)], the selected Cu(hfac)$_2$-D structure displaying the bond baths and critical points. Atom critical points (ACPs, white), Ring critical points (RCPs, green), and Bond critical points (BCPs, red).

The radical ion salt with the first packing contains two units of donor D: Me_3TTF-CH=CH-Pyr and three acceptors A: PF_6^- named 2D-3A. They show the existence of BCPs, RCPs, and some additional intramolecular/intermolecular interactions abbreviated as the D-D, the D-A, and the H…H interactions (Figure 13). The intermolecular interactions responsible for the donor packing are of two types. The first type symbolized by D-D is exhibited as N56⋯H103-C, N-C14⋯H98-C, and N37⋯H93-C interactions, with distances 2.935, 3.159, and 3.168 Å, respectively. The second type (D-A) is given as BCPs connections; F72⋯S51, H121⋯F74, H115⋯F74, S31⋯F74, S31⋯F75, H108⋯F75, H108⋯F73, C48⋯F73, S51⋯F73, S52⋯F73, F28⋯S31, F23⋯H86, F23⋯S2, F23⋯S30, F23⋯S31, F24⋯H107, F27⋯H119, F25⋯S3, and F25⋯S2, with the corresponding distances 3.403, 2.536, 2.289, 3.480, 3.394, 2.446, 2.872, 3.252, 3.442, 3.378, 3.316, 2.461, 3.349, 3.517, 3.593, 2.638, 2.471, 3.694, and 3.245 Å, respectively. The intramolecular interactions found in the donors themselves are abbreviated as H⋯H, given as H90⋯H92, H80⋯H118, H94⋯H95, H94⋯H109, H8⋯H84, H81⋯H85, H110⋯H113, and H110⋯H114 with distances 2.094, 2.064, 2.141, 2.068, 2.044, 2.135, 2.148, and 2.152 Å, respectively. Some of these additional interactions are responsible for the stability and crystal packing. According to the obtained ρ_{BCP}, $\nabla^2\rho_{BCP}$, and HBCP values (Summarized in supporting information), all of these interactions suggest weak interactions with an electrostatic character. This is confirmed by $\nabla^2\rho_{BCP} > 0$ and $H_{BCP} > 0$. We note a very high Ellipticity in most of the RCPs (approximately 60.65), which suggests a high degree of π-characteristics. The low value of Ellipticity indicates that this interaction is a bond with negligible character.

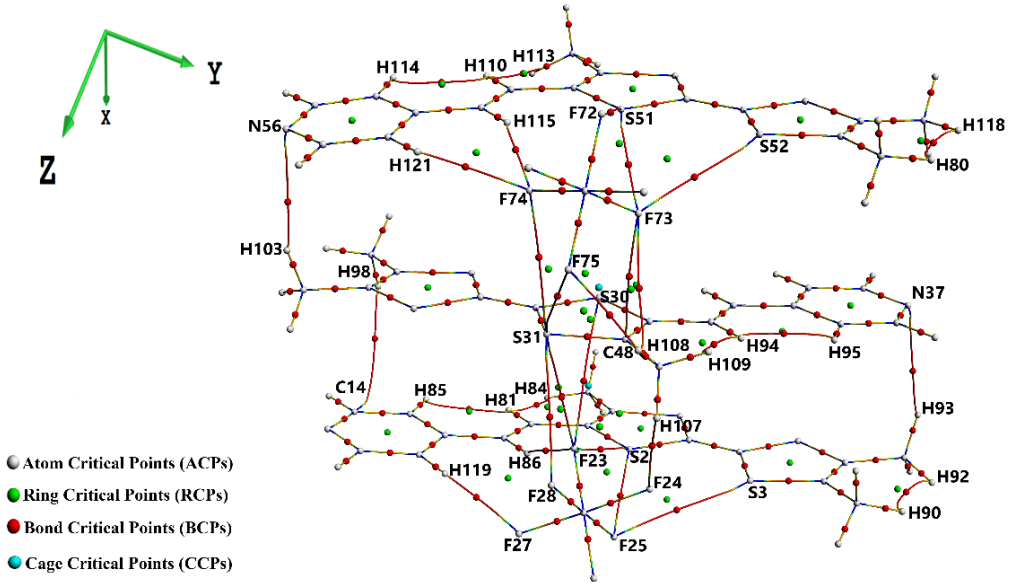

Figure 13: $(Me_3TTF\text{-}CH{=}CH\text{-}Pyr)_2(PF_6)_3$ (2D-3A) structure with Atom critical points (ACPs, white), Ring critical points (RCPs, green), Bond critical points (BCPs, red), and Cage critical points (CCPs, blue).

4.5. Molecular Electrostatic Potential (MEP)

The Molecular Electrostatic potential map is a very useful tool that allows the visualization of the charge distributions, the size, and the shape of molecules. It is also a very useful descriptor for determining the possible regions for radical, nucleophilic, and electrophilic attacks, as well as hydrogen bonding interactions in a molecular system [43]. These regions' sites are demonstrated by different colors; from red to blue. At a given point p(x,y,z), The MEP (V(r)) is defined as the force acting on a positive test charge (a proton) located at p (r) through the electrical charge cloud generated through the molecule's electrons and nuclei. For the title compounds, the MEP V(r) values were calculated as described previously using the following formula: [44]

$$V(r) = \sum_A \frac{Z_A}{(R_A - r)} - \int \frac{\rho(r')}{(r' - r)} dr' \qquad (1)$$

The electrostatic potential that is created in the space around a molecule by its nuclei and electrons, Z_A is the charge of the nucleus allocated at R_A, $\rho(r')$ is the electron density function of the molecule, and r' is the dummy integration variable. Calculated molecular electrostatic potential (MEP) map of the ligand and the complex at different oxidation states; from 1+ to 4+ are illustrated in Figure 14. The red color represents the most reactive site for a possible electrophilic attack, while the deep blue for a possible nucleophilic attack. The more red/blue differences, the more polar the molecule. The peripheral hydrogen atoms in the uncoordinated ligand are the probable sites for the nucleophilic attack. While the oxygen atoms are the favored sites for the electrophilic attack. On the (Me_3TTF-CH=CH-Pyr) unit, the neutral potential represented by green regions is concentrated around the carbon atoms. This color disappears and becomes yellow after coordination (Figure 14-a). When increasing the oxidation degree up to 3+, this color disappears mostly from the TTF side, it becomes green with a neutral potential. The $Cu(hfac)_2$ regions at the 3rd and the 4th oxidation states are characterized with deep red, confirming that the electron extraction is from the Cu ion, it is also illustrated by bond length values and the Hirshfeld charges. From the MEP map of the $[Cu(hfac)_2(L)]^{4+}$ hybrid-ligand complex, the deepest yellow and red dominate most of the complex regions (Figure 14-f).

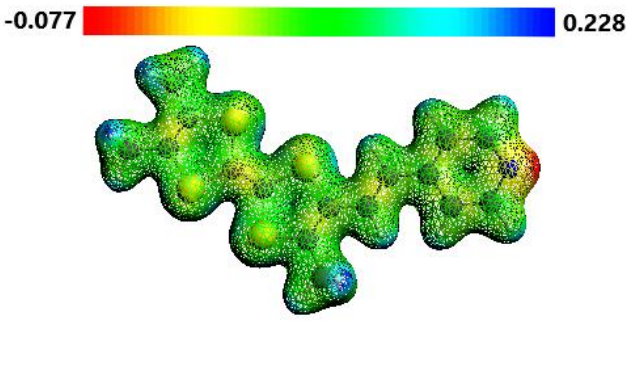

(a)

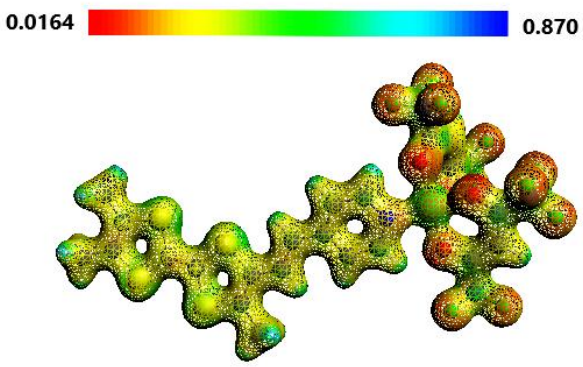

(b)

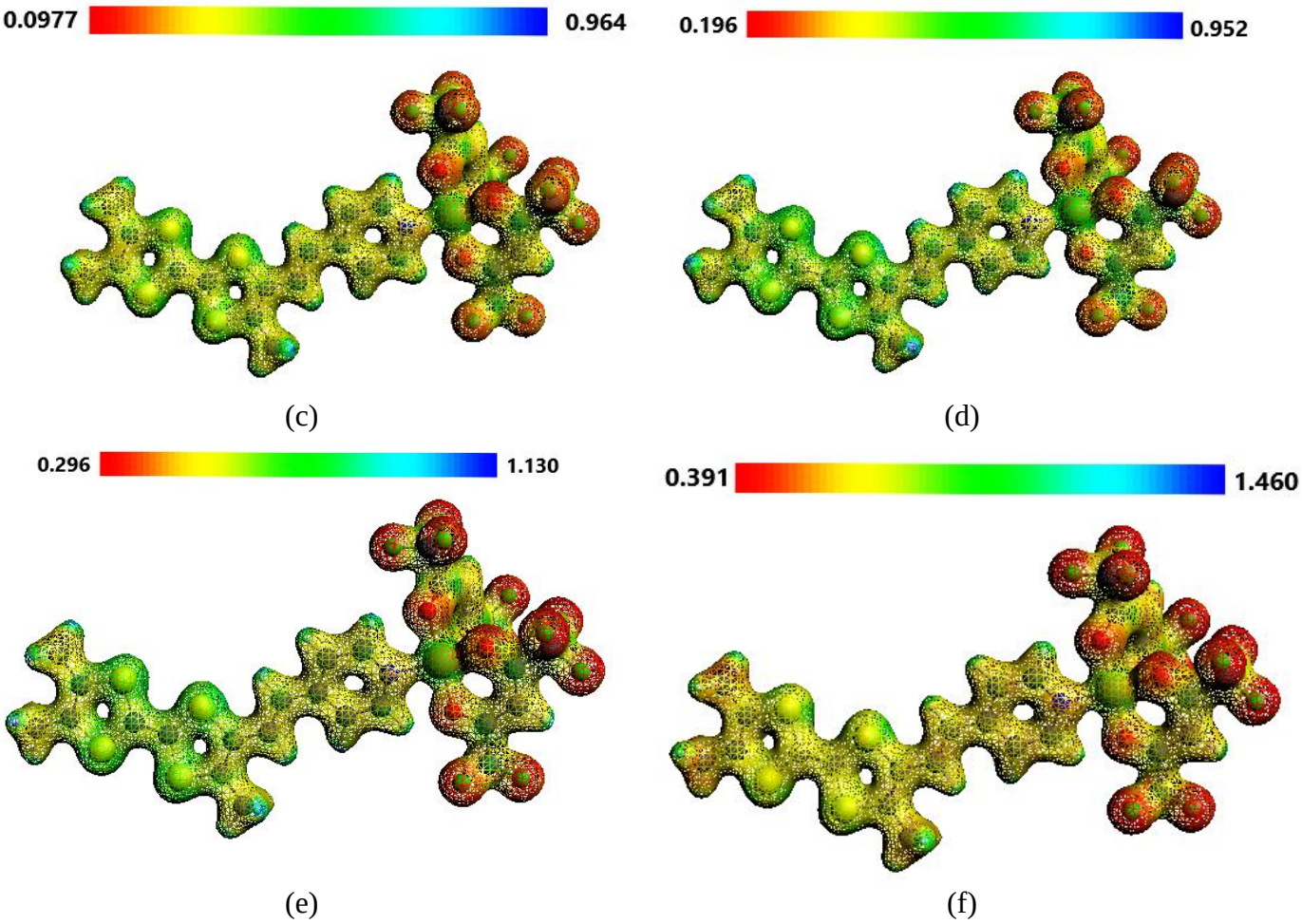

Figure 14: Molecular electrostatic potential map of (Me_3TTF-CH=CH-Pyr) ligand (a), $[Cu(hfac)_2(L)]^0$ (b) $[Cu(hfac)_2(L)]^{1+}$ (c), $[Cu(hfac)_2(L)]^{2+}$ (d), $[Cu(hfac)_2(L)]^{3+}$ (e), and $[Cu(hfac)_2(L)]^{4+}$ (f).

4.6.Non-Covalent Interactions

It is crucial to understand non-covalent interactions (NCI) as they play a key role in solving various chemical and biological problems. They are used in many areas of theoretical chemistry and related disciplines, such as material science and biochemistry [45–48]. This index is a valuable tool for pinpointing the common interaction regions within a molecular structure, such as van der Waals interactions (vdW) and hydrogen bonds (HBs). It relies on electron density studies, providing a semi-quantitative representation of these interactions. Furthermore, it is minimally affected by the method

and basis set used for electron calculation, with variations primarily stemming from changes in the geometry [49]. The non-covalent interactions in the title hybrid-ligand complex are represented in Figure 15, with the color code showing repulsive interactions in deep red and attractive interactions in deep blue. The hybrid-ligand complex represents two types of interactions on the electronic density range of $0.003 < \rho < 0.015$. Week repulsive represented by the yellow regions are mainly located between the sulfur atoms of the TTF core; S(4)···S(2) and S (3)···S(1). The stabilization interaction between the oxygen atoms (O(4)···O(2), O(4)···O(3), and O(2)···O(1)) of the hfac moieties is due to the mesomeric effect. The green color represents regions of weak attractive interactions, mainly located between S(1)···H(8), O(1)···H(12), O(4)···H(11), F(7a)···H(24), F(12a)···H(24), and H(7)···C(9). These later are assigned to weak H-bonding interactions. The NCI index is in good agreement with the QTAIM results; it shows similar positions of the weak hydrogen bonding (HBs) and H-H interactions.

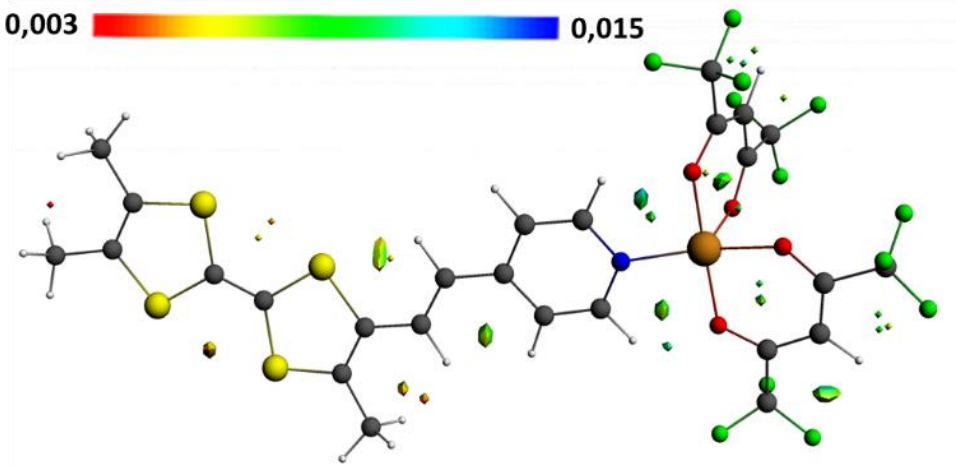

Figure 15: 3D NCI plot of the hybrid-ligand complex (computed at the PBE/TZP level of theory). The gradient isosurfaces (s = 0.03 a.u.) over the range 0.003 - 0.015a.u.).

4.7. Global Reactivity Descriptors

The chemical reactivity and site selectivity of molecular systems can be effectively understood using conceptual density functional theory (DFT). Parameters such as Ionization potential (I) (eV), Electron affinity (A) (eV), Electronegativity (χ) (eV), Electrochemical potential (μ) (eV), Global chemical hardness (η) (eV), Global chemical softness (S) (eV^{-1}) and Electrophilicity index(ω) (eV) are important

for predicting trends in overall chemical reactivity. These parameters provide information on the chemical stability of the compounds, they are mainly based on the energies of the HOMO – LUMO orbitals. According to the Koopmans theorem, the ionization potential (I) and electron affinity (A) can be defined by the following equations [50]:

$$I = -\mathrm{E_{HOMO}} \qquad A = -\mathrm{E_{LUMO}} \qquad (2)$$

The absolute electronegativity (χ) is defined as [50,51]:

$$\boldsymbol{\chi = -\mu = -\,{}^{1}\!/_{2}\,(E_{LUMO} + E_{HOMO})} \qquad (3)$$

The electronic chemical potential (μ) and chemical hardness (η) are calculated as follows:

$$\mu = {}^{1}\!/_{2}\,(E_{LUMO} + E_{HOMO}) \qquad (4)$$

$$\eta = (E_{LUMO} - E_{HOMO}) \qquad (5)$$

The global softness (S) is defined as the inverse of the global hardness (η):

$$S = {}^{1}\!/_{\eta} \qquad (6)$$

The global electrophilicity index (ω) as introduced by Parr et al. [52] can be defined as:

$$\omega = {}^{\mu^2}\!/_{2\eta} \qquad (7)$$

The Global Reactivity Descriptors were examined based on the optimization of complex structure; the results are summarized in Table 8.

Table 8: Global reactivity indices of [Cu(hfac)$_2$(Me$_3$TTF-CH=CH-Pyr)] at the neutral and the oxidized states.

Parameters	E_S **(eV)**	E_L **(eV)**	A **(eV)**	I **(eV)**	μ **(eV)**	η **(eV)**	ω **(eV)**	χ **(eV)**	S **(eV^{-1})**
					α-Spin				
$[Cu(hfac)_2(L)]^0$	-4.560	-3.546	3.546	4.560	-4.053	1.014	8.100	4.053	0.986
$[Cu(hfac)_2(L)]^{1+}$	-7.481	-6.332	6.332	7.481	-6.906	1.149	20.757	6.907	0.8703
$[Cu(hfac)_2(L)]^{2+}$	-10.474	-10.459	10.459	10.474	-10.467	0.015	3651.587	10.467	66.667

$[Cu(hfac)_2(L)]^{3+}$	-13.196	-13.167	13.167	13.196	-13.182	0.029	2995.723	13.182	34.483
$[Cu(hfac)_2(L)]^{4+}$	-16.505	-15.881	15.881	16.505	-16.193	0.624	210.107	16.193	1.603
				β-Spin					
$[Cu(hfac)_2(L)]^{0}$	-4.546	-4.486	4.486	4.546	-4.516	0.060	169.952	4.516	16.667
$[Cu(hfac)_2(L)]^{1+}$	-7.730	-7.628	7.628	7.730	-7.679	0.102	289.054	7.679	9.804
$[Cu(hfac)_2(L)]^{2+}$	-10.784	-10.113	10.113	10.784	-10.449	0.671	81.349	10.449	1.490
$[Cu(hfac)_2(L)]^{3+}$	-13.465	-13.236	13.236	13.465	-13.351	0.229	389.161	13.351	4.367

Where: E_S = E(SOMO), E_L=E(LUMO), L: Me_3TTF-CH=CH-Pyr

The more we increase the degree of oxidation of the present hybrid-ligand complex, the more it becomes more difficult to remove their electrons. The hybrid-ligand complex becomes more stable, as confirmed by the ionization potential (I) and the negative values of the electrochemical potential μ. It is worth noting that the ionization potential values are very close to the electronic affinity (A) values in both alpha and beta spins. This indicates that the energy required to remove one electron from this molecule is almost equal to the energy released when adding an electron to the neutral state of the molecule. The present hybrid-ligand complex shows an excellent electrophilic property; $[Cu(hfac)_2(L)]^{2+}$, $[Cu(hfac)_2(L)]^{3+}$ and $[Cu(hfac)_2(L)]^{4+}$ with the values (3651.587 eV, 2995.723 eV, and 210.107 eV), respectively, which explains its ability to form different stable materials (ion-radical salts). The $[Cu(hfac)_2(L)]^{2+}$ and $[Cu(hfac)_2(L)]^{3+}$ structures show a high polarizability and chemical reactivity confirmed by a high softness and lowest gap energy values. Furthermore, the energy gap in the alpha spin at the (0, 1+, 4+) states is greater than the beta spin at all the other states, as confirmed by their hardness values. As a result, they have low chemical reactivity but a high kinetic susceptibility. We note that the hybrid-ligand complex with alpha spin is more reactive than with beta spin Additionally, this compound will not spontaneously decompose into its elements because of their negative electrochemical potential and moderate ionization energy levels.

4.8. Local reactivity descriptors

These descriptors are used to measure the reactivity on specific sites of a molecule. The most important indicator is the Fukui function f(r) proposed in 1984 by Parr and Yang [53]. They mentioned that the

sites with higher values of the Fukui function [54] (f_k) are more prone to reactivity under the corresponding types of attack. The corresponding proposed expressions (Eq 8 to Eq 10) have been tested on the title hybrid-ligand complex, using the Hirshfeld atomic charges and the conceptual Density Functional Theory (DFT).

For electrophilic attack:

$$f_k^+ = q_k(N+1) - q_k(N) \qquad (8)$$

For nucleophilic attack:

$$f_k^- = q_k(N) - q_k(N-1) \qquad (9)$$

For radical attack:

$$f_k^0 = {}^1/_2\,(q_k(N+1) - q_k(N-1) \qquad (10)$$

Where $q_k(N)$, $q_k(N-1)$, and $q_k(N+1)$, are the electronic population of k atom in neutral, anionic, and cationic molecule respectively.

The results presented in Table 9 were carried out in the gas phase using the single-point calculation performed at the same level of theory as the optimization. These calculated values indicate that the sulfur atoms are the most susceptible to nucleophilic, electrophilic, and free radical attacks. Furthermore, the ethylenic C2, C8, and C11 sites are reactive towards electrophilic attacks, while the C2 and C8 are also prone to free radical attack.

Table 9: The reactive sites for non-hydrogen atoms in the [Cu(hfac)$_2$(Me$_3$TTF-CH=CH-Pyr)].

Atom	f_k^+	f_k^-	f_k^0	Atom	f_k^+	f_k^-	f_k^0	Atom	f_k^+	f_k^-	f_k^0
C15	0.011	0.007	0.009	C13	0.012	0.032	0.022	F8a	0.003	0.000	0.0015
C5	0.026	0.012	0.019	C12	0.012	0.035	0.0235	F7a	0.009	0.007	0.008
C6	0.026	0.013	0.0195	N1	0.013	0.037	0.025	F9a	-0.006	0.006	0.000
C16	0.012	0.008	0.010	C11	0.012	0.045	0.0285	O1	0.002	-0.010	-0.004
S4	0.090	0.044	0.067	C10	0.013	0.030	0.0215	O2	0.009	0.007	0.008
S3	0.084	0.040	0.062	Cu	0.031	0.000	0.0155	C18	0.007	0.004	0.0055
C4	0.024	0.022	0.023	O3	0.015	-0.001	0.007	C19	0.011	0.009	0.010

C3	0.031	0.001	0.016	O4	0.006	-0.007	-0.0005	C17	0.004	0.002	0.003
S2	0.072	0.083	0.0775	C25	0.008	0.005	0.0065	F1	0.003	-0.002	0.0005
S1	0.079	0.024	0.0515	C24	0.010	0.006	0.008	F2	0.005	0.004	0.0045
C2	0.015	0.056	0.0355	C26	0.006	0.003	0.0045	F3	0.009	0.008	0.0085
C1	0.018	0.019	0.0185	F10a	0.007	0.003	0.005	C20	0.010	0.009	0.0095
C14	0.01	0.016	0.013	F11a	0.006	0.004	0.005	C21	0.005	0.004	0.0045
C7	0.009	0.052	0.0305	F12a	0.009	0.008	0.0085	F4	0.009	0.007	0.008
C8	0.026	0.047	0.0365	C23	0.007	0.002	0.0045	F5	0.006	0.005	0.0055
C9	0.045	-0.002	0.0215	C22	0.004	0.002	0.003	F6	0.007	0.005	0.006

4.9. Bond Energy Decomposition Analysis

The Bond Dissociation Energy (BDE) method, developed by Ziegler and Rauk, [55] involves a DFT calculation. In the main work, the BDE calculation was performed on the isolated fragments; (Me_3TTF-CH=CH-Pyr) and Cu(hfac)$_2$ to analyze the relative stability and the nature of the Cu-N-bonds in both neutral and oxidized states. The total binding energy is divided into three terms: Pauli energy $\Delta E_{pauli,}$ which refers to the repulsive interactions between fragments; orbital energy $\Delta E_{orb,}$ which mainly explains the interaction between occupied and vacant orbitals; and the ΔE_{elec}, which represents the electrostatic interaction energy between these fragments. The electrostatic and Pauli repulsion energies are grouped under the term steric energy, which is the sum of steric and Pauli's orbital energy. The total binding energy BDE (ΔE_{Tot}) is defined by the following equation [56]:

$$\boldsymbol{BDE} = \Delta \boldsymbol{E_{ele}} + \Delta \boldsymbol{E_{pauli}} + \Delta \boldsymbol{E_{orb}} = \Delta \boldsymbol{E_{orb+pauli}} + \Delta \boldsymbol{E_{ele}} \quad (11)$$

The various contributions of the binding energy, besides the type of the corresponding bonds between pairs of fragments are grouped in Table 10. It is observed that the Cu-N bond has an ionic contribution in the neutral state. The covalency of the bond increases as the oxidation state increases, from 2.32% at the 1+ state to 43.38% at the 4+ oxidation state. The stability of this bond also increases with the oxidation state. These results can be explained by the distribution of electron clouds on the Cu-N bond in the non-neutral states, as well as the increase in the positive charge of the copper metal as the oxidation state changes from 0.427 e- to 0.521 e-.

Table 10. Energies (eV) of decomposition of the Copper-Nitrogen bond in the hybrid-ligand complex of general formula $[Cu(hfac)_2(Me_3TTF\text{-}CH{=}CH\text{-}Pyr)]^{n+}$.

	BDE	Covalent (%)	Ionic (%)
$[Cu(hfac)_2(L)]^0$	-2.24	2.32	97.68
$[Cu(hfac)_2(L)]^{1+}$	3.60	8.27	91.73
$[Cu(hfac)_2(L)]^{2+}$	12.77	17.44	82.56
$[Cu(hfac)_2(L)]^{3+}$	24.57	28.93	71.07
$[Cu(hfac)_2(L)]^{4+}$	38.82	43.38	56 .62

L: $Me_3TTF\text{-}CH{=}CH\text{-}Pyr$. n: oxidation degree ($0 \leq n \leq 4$).

4.10. Vibrational analysis

The infrared spectra of the experimental ($Me_3TTF\text{-}CH{=}CH\text{-}Pyr$) ligand and the $[Cu(hfac)_2(Me_3TTF\text{-}CH{=}CH\text{-}Pyr)]$ hybrid-ligand complex were obtained using the ATR mode. The fundamental vibrational wavenumbers of these compounds were calculated at the same level as the optimization. The calculated IR spectra of the optimized structures are shown in Figures 16-a and 16-c, while the experimental ones are illustrated in Figures 16-b and 16-d. It's worth mentioning that all the vibrational bands characteristic of the title compounds are positive, which may indicate the stability of these later. Additionally, there is a good agreement observed between theoretical and experimental spectra.

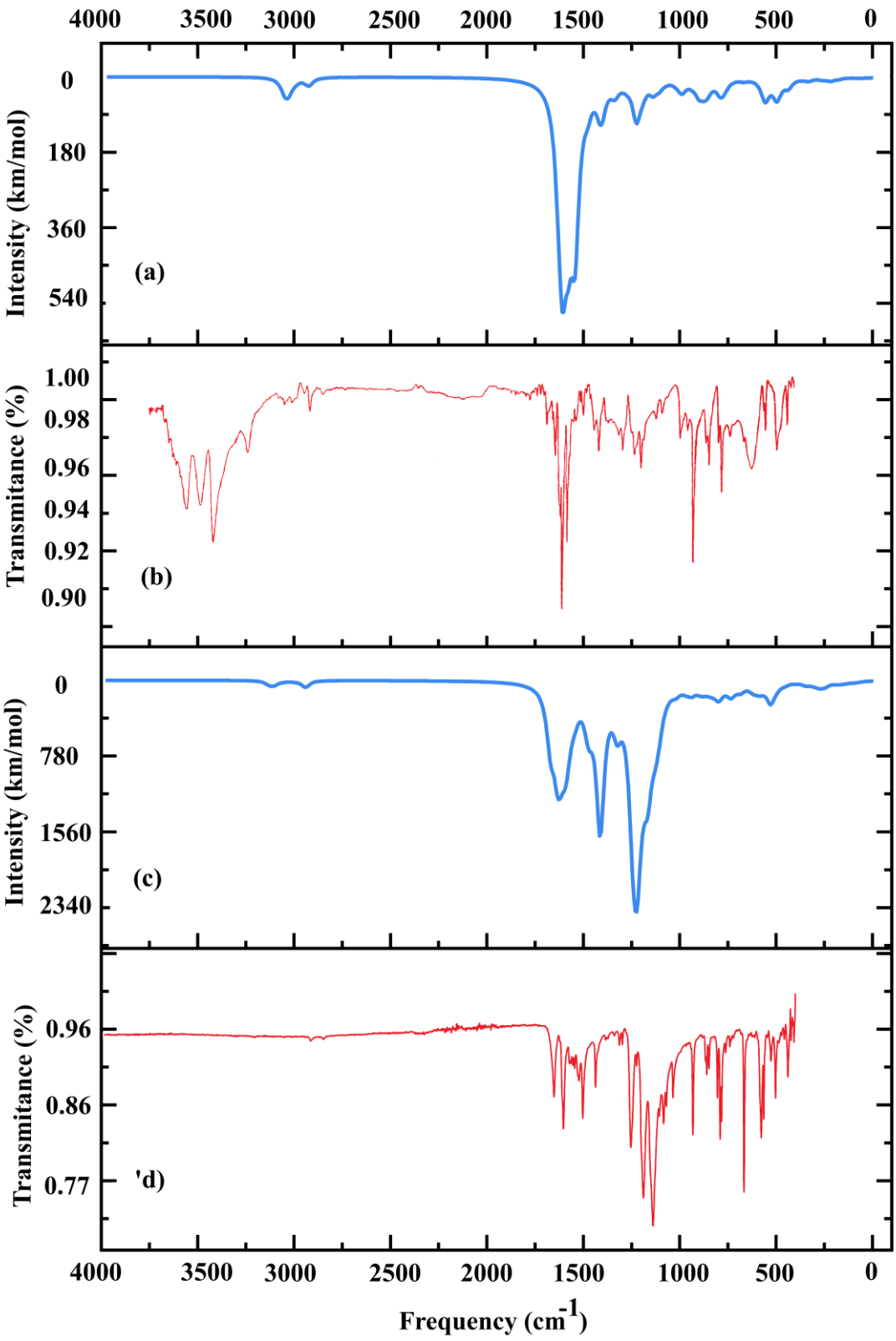

Figure 16: Experimental (in red) and Theoretical (in blue) FTIR spectra of the ligand Me_3TTF-CH=CH-Pyr (a, b) and the corresponding hybrid-ligand complex [Cu(hfac)$_2$(Me_3TTF-CH=CH-Pyr)] (c, d).

(Me_3TTF-CH=CH-Pyr) vibrations

The ligand spectrum contains bands corresponding to C–H, C–C, C–C–C, and H–C–C bending, as well as C–C–C–C torsion vibrations, due to the vinyl pyridine unit. The torsional vibration frequency of the C–C–C bond was previously reported at 1216 cm^{-1} by H. Ghanem et al. [57], whereas in our current study, it is observed at 1205 cm^{-1}. The modes calculated at 2936 and 3044 cm^{-1} are identified as symmetric and asymmetric C–H stretching modes, respectively. The observed wavenumbers in the experimental spectrum occur at 2915 cm^{-1} and 2849 cm^{-1}, in good agreement with the literature [58,59]. In-plane C–H bending vibrations are related to C–C stretching vibrations and the vibrations of the aromatic compound have been reported in the range 1500–1100 cm^{-1} [60,61]. In the current study, absorption peaks were detected at 1471 cm^{-1} which falls within the expected experimental range 1500-1484 cm^{-1}. Out of plane C–H bending vibrations were observed in the range 811-884 cm^{-1}, while in the experimental spectrum, they were found to be in the range of 908-811 cm^{-1}. These values closely match to those reported by O. Khaoua et al. [61]. The C=C stretching vibration modes are calculated in the 1542–1416 cm^{-1} region, and they are observed in the experimental spectrum in the range of 1501-1436 cm^{-1}. The aromatic =C-N= stretching vibration mode is observed at the wavenumber range 1441-1412 cm^{-1}, which aligns the experimental spectrum in 1466-1418 cm^{-1} (previously reported at 1398 cm^{-1} [62]). The C–S stretching vibrations are calculated in the wavenumber range of 930–734 cm^{-1} and they are observed in the experimental spectrum at 928-741 cm^{-1}, which is close to the reported range of 942-752 cm^{-1} [63]. The comparison of these two spectra affirms the good approximation of the computation study. However, in the experimental ligand spectrum, three bands characteristic of the N-H stretching vibration were observed at the range 3600-3300 cm^{-1} (previously reported in the range of 3698-3150 cm^{-1} [63]). This can be explained by the high reactivity of the nitrogen of the pyridine ring, which causes the capture of hydrogen from the air.

[$Cu(hfac)_2$(Me_3TTF-CH=CH-Pyr)] vibrations

When (Me_3TTF-CH=CH-Pyr) is coordinated with $Cu(hfac)_2$, certain bands disappear and new ones appear. In both the experimental and theoretical spectra, the characteristic N-H band disappears, while a new vibration related to the copper (II) environment emerges. The -C-O- stretching mode from the hfac part occurs strongly in the range 1646-1636 cm^{-1} in the theoretical spectrum, but in the experimental spectrum, it appears in the region 1651-1602 cm^{-1}. which is close to the reported values of 1652-1623 [63]. The corresponding deformation mode is calculated at 1325 cm^{-1}, but it appears in the experimental spectrum at 1339-931 cm^{-1}. The Cu–O stretching vibrations of the hfac part occur at the wavenumber 542 cm^{-1} and are observed in the experimental spectrum at 527 cm^{-1} (previously found at 539 [64]). The calculated and the experimental Cu–N stretching vibrations wavenumber fall in the ranges 595-583 cm^{-1} and 592-577 cm^{-1}, respectively. The calculated C–F stretching vibrations occur at 1212 cm^{-1}, while in the experimental spectrum, they are found at 1252 cm^{-1}.

4.11. UV-Visible spectroscopy analysis

The UV-Vis absorption spectrum of [$Cu(hfac)_2$(Me_3TTF-CH=CH-Pyr)] was measured in CH_2Cl_2 with the absorption peaks ranged from 220 nm to 800 nm. In the UV-Vis absorption spectrum presented in Figure 17-b-, the hybrid-ligand complex exhibited a strong and sharp absorption peak at 314 nm, indicating the π-π* transitions of the TTF moiety. The absorption peak generated at 436 nm may correspond (ascribing) to the n-π* transitions. To gain a deeper understanding of the electronic transitions, the ligand and the corresponding copper complex at the neutral and oxidized states were characterized spectroscopically using the Time-Dependent DFT method (TD-DFT) [32] at the PBE/TZP/SAOP level [33]. This method allows determining the nature of the most important electronic transitions, electronic excitation energies, and their oscillating strengths. The calculated electronic spectra for these compounds are illustrated in Figure 17 (a, b, d, e, f, g). The simulated spectra (Figure 17-a-) and (Figure 17-c-) revealed that the charge transfer bands are red-shifted (Bathochromic effect) in the neutral hybrid-ligand complex (Figure 17-c-) compared with the spectrum of the free ligand (a). The first band at 405 nm is shifted to 432 nm and the second one at 865 nm is shifted to 977 nm. This first band wavelength value (of 405 nm) is close to that

reported for the TTF unit around 410 to 440 nm [64–69]. Additionally, the appearance of two other bands at 591 nm and 796 nm in the neutral hybrid-ligand complex was observed. With an increase in the oxidation degree, the band absorption at 865 nm in the neutral hybrid-ligand complex spectrum experienced a blue-shift (Hypochromic effect). For the free ligand (Me_3TTF-CH=CH-Pyr), the first absorption band at 405 nm (0.035 eV) corresponds to the transition HOMO-1 → LUMO, while the second absorption band at 865 nm (0.043 eV) is due to the transition HOMO → LUMO. These two characteristic electronic transitions are described as intramolecular charge transfers $\pi \rightarrow \pi^*$ from the TTF to the pyridine vinylic, as reported in previous works [63,70].

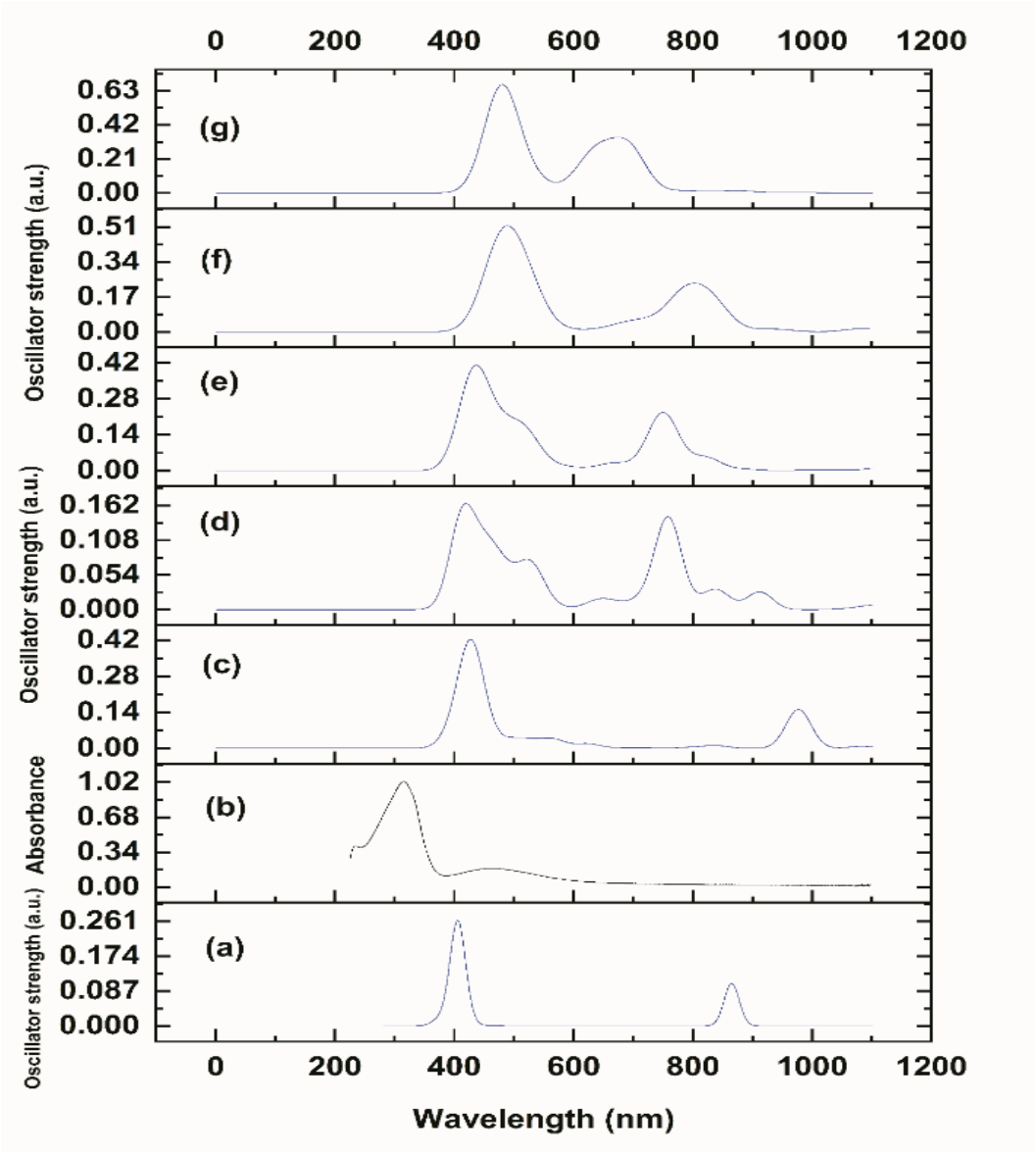

Figure 17: Theoretical absorption spectra of L= (Me_3TTF-CH=CH-Pyr) ligand (a), $[Cu(hfac)_2(L)]^0$ (c), $[Cu(hfac)_2(L)]^{1+}$ (d), $[Cu(hfac)_2(L)]^{2+}$ (e), $[Cu(hfac)_2(L)]^{3+}$ (f), $[Cu(hfac)_2(L)]^{4+}$ (g) hybrid-ligand complexes, and experimental absorption spectrum of $[Cu(hfac)_2(L)]^0$ hybrid-ligand complex (b).

The results of the major electronic transition and the concerned orbitals are collected in supporting information. The excitation mechanism of the $[Cu(hfac)_2(L)]^0$ hybrid-ligand complex exhibits four absorption bands at 432 nm, 591 nm, 796 nm, and 977 nm, the first frequency being the most intense. The band of wavelength 591 nm is close to the reported one at 603 nm by S. Belhouchat et al. [63]. Table 11 includes wavelength λ (nm), large values of oscillator strength (f), the composition of excited states, and the character of electronic transitions.

Table 11: Selected calculated values λ_{calc} , total energy (E eV), Oscillator strength (Osc f), Composition (Compo %), the electronic transition and their character are reported for the title compounds.

	λ_{calc} (nm)	**E (eV)**	**Osc (f)**	**Comp (%)**	**Transition**			**Character**
L^0	865	0.106	0.106	91.7	HOMO	→	LOMO	ILCT
	405	0.240	0.264	61.2	HOMO-1	→	LOMO	ILCT
$[Cu(hfac)_2(L)]^0$	977	1.014	0.151	47.4	HOMOα	→	LUMOα	ILCT
	624	2.179	0.016	97.6	HOMOα-2	→	LUMOα	ILCT+ MLCT
	516	2.344	0.015	84.5	HOMOβ-6	→	LUMOβ	ILCT
	436	2.721	0.038	39.2	HOMOα	→	LUMOα+5	ILCT
$[Cu(hfac)_2(L)]^{1+}$	912	1.658	0.027	78.9	HOMOβ-3	→	LUMOβ	MLCT+ LLCT+ ILCT
	840	0.940	0.027	89.0	HOMOβ-2	→	LUMOβ	LLCT
	761	1.496	0.118	42.7	HOMOα-1	→	LUMOα	ILCT
	655	1.889	0.004	95.6	HOMOα-3	→	LUMOα	MLCT+ LLCT
	528	3.500	0.034	39.9	HOMOα-10	→	LUMOα	LLCT+ ILCT
	432	2.932	0.0009	48.4	HOMOα-1	→	LUMOα+5	ILCT
$[Cu(hfac)_2(L)]^{2+}$	821	1.293	0.051	40.1	HOMOβ-3	→	LUMOβ	LLCT+ ILCT
	753	1.550	0.164	47.5	SOMOα	→	LUMOα+1	LLCT+MLCT
	664	1.807	0.015	81.3	HOMOβ	→	LUMOβ+2	LLCT+ MLCT
	516	2.030	0.042	41.4	HOMOα-8	→	LUMOα	MMCT+ MLCT+ ILCT+ LLCT
	444	2.838	0.005	67.5	HOMOα-2	→	LUMOα+3	LLCT+ MLCT
$[Cu(hfac)_2(L)]^{3+}$	807	1.467	0.239	50.2	HOMOβ-1	→	LUMOβ+2	MMCT+ ILCT
	706	1.743	0.061	63.1	HOMOβ-5	→	LUMOβ+1	MLCT+ LLCT
	494	1.183	0.519	68.4	HOMOβ-3	→	LUMOβ	ILCT
$[Cu(hfac)_2(L)]^{4+}$	858	1.500	0.005	70.7	HOMOβ-3	→	LUMOβ+1	LLCT+ LMCT
	671	1.847	0.014	53.3	HOMOβ-7	→	LUMOβ	LMCT+ LLCT
	475	2.699	0.668	88.9	HOMOβ-10	→	LUMOβ+1	LLCT+ LMCT

It can be assigned to the same transition of the free ligand; from the HOMO-1 to LUMO. The $[Cu(hfac)_2(L)]^{1+}$ compound shows absorption bands at 577 nm and 675 nm, while the $[Cu(hfac)_2(L)]^{2+}$ compound has absorption bands at 512 nm and 739 nm (previously found at 731 nm) [63], These are assumed to be more intense compared to the neutral hybrid-ligand complex $[Cu(hfac)_2(L)]^0$. Furthermore, the $[Cu(hfac)_2(L)]^{3+}$ (f) and $[Cu(hfac)_2(L)]^{4+}$ (g) compounds exhibit two characteristic absorption bands. The first absorption bands are located at 494 nm and 807 nm, which refer to the electronic excitation arising from HOMO-14 to LUMO (68.4%) and from HOMO-1 to LUMO+2 (50%), respectively. The second absorption bands are located at 475 nm and 695 nm, representing the electronic excitation HOMO-10→ LUMO+1 (88.9%) and HOMO-2→ LUMO+2 (41.8%), respectively. The maximum value of the oscillator strength was reached for the $[Cu(hfac)_2(L)]^{4+}$ structure, with the first calculated band at 475 nm (f = 0.668 a.u), representing the electronic transition HOMO-10 → LUMO+1 (88.9 %). The low value was recorded for the neutral structure, with the calculated band at 796 nm (f = 0.013 a. u.), representing the electronic transition HOMO-3→ LUMO (98.4%).

5. Conclusion

Based on our findings, we have discovered that copper (II) is a suitable metal ion capable of forming interesting molecular structures. The tetrathiafulvalene (TTF) component has a diverse field of applications in molecular electronics and supramolecular chemistry. In this study, we conducted both experimental and computational DFT analyses on the redox-active trimethylethenylpyridyl-tetrathiafulvalene. It was covalently coordinated with the $Cu(hfac)_2$ framework to create a new hybrid material $[Cu(hfac)_2(Me_3TTF\text{-}CH{=}CH\text{-}Pyr)]$. Our structural analysis proved to be invaluable in understanding the physical properties, aiding in the design of these compounds. The theoretical studies further helped in explaining the available experimental data, including the chemical and biological properties. The crystal structure analysis using single-crystal X-ray diffraction revealed that the metal ion is in a deformed pyramid with a square base. Besides, we examined the different spin distributions in the neutral and oxidized pseudo-pyramidal Cu^{II} complex with charges ranging from +1 to +4. We found that

applying a +1 and +2 charges to the Cu^{II} complex in the exclusion of the metal spin, indicating a pair of missing electrons from the ylidene part; C_2S_4 of the TTF unit. This unique feature may lead to interactions such as possible π-π stacking between ligands of different complexes in crystals. We also examined the electronic properties of (Me_3TTF-CH=CH-Pyr) and the corresponding Cu^{II} hybrid-ligand complex. The molecular charge, spin distributions, and TD-DFT calculations of these two structures exhibited an intense and multiplex charge transfer, including MLCT, ILCT, and LLCT, and a low bandgap energy of the complex, indicating potential for improved redox properties and suitability for photoelectron conversion materials. This is confirmed by the cyclic voltammetry which reveals the presence of two reversible oxidation states associated with the TTF ligand. Additionally, the vibrational calculation showed the absence of the imaginary values, which indicate the stability of the compounds, which aligns well with the experimental FTIR spectrum. The NCI analysis revealed short S···S contacts on the (Me_3TTF-CH=CH-Pyr) side, along with CH···O, and O···O interactions. This finding is confirmed by Atom in molecule analysis, which is also in good agreement with the X-ray data. The MEP analysis identified the external H atoms of the ligand unit as potential sites for a nucleophilic attack, while the oxygen and fluorine atoms from the hfac side are favored sites for an electrophilic attack due to their negative potential. Furthermore, the local reactivity descriptors calculated using the Fukui functions indicate that C2, C8, and C11 are the reactive sites for electrophilic attacks, and the sulfur atoms are prone to all attack types. The global reactivity descriptors indicate that the complex with alpha spin is more reactive because of its excellent electrophilic index, high softness, and polarizability, in comparison to the complex with beta spin, which is a good electrophile but has very low softness.

Author Contributions

HS executed the research, optimized methods, and participated in conceptualizing the study; OK participated in conducting the experimental characterization and theoretical investigation, analyzed data, drafted and revised the manuscript; SZ participated in conducting the study, entering data and drafting

the manuscript; NB conceived the study, wrote the manuscript, and supervised the study; AG revised the manuscript; and SG solved and refined the crystallographic data and performed the experimental structural analysis. All authors read and approved the final manuscript submission.

Conflicts of interest

There are no conflicts to declare.

Acknowledgments

The authors wish gratefully to express thanks to the DGRSDT and the Algerian Ministry of Higher Education and Scientific Research for PRFU Project (B00L01UN050120180007). X–Ray data collection was performed at the Centre de Diffractométrie X from the Institut des Sciences Chimiques de Rennes (UMR 6226 Université de Rennes – CNRS). All authors thank Pr. Lahcène Ouahab for the data collection.

References

[1] R. Luebke, Y. Belmabkhout, Ł.J. Weseliński, A.J. Cairns, M. Alkordi, G. Norton, Ł. Wojtas, K. Adil, M. Eddaoudi, Versatile rare earth hexanuclear clusters for the design and synthesis of highly-connected ftw -MOFs, Chem Sci 6 (2015) 4095–4102.

[2] W.G. Cui, T.L. Hu, X.H. Bu, Metal–Organic Framework Materials for the Separation and Purification of Light Hydrocarbons, Advanced Materials 32 (2020) 1806445.

[3] S. Chen, Z. Song, J. Lyu, Y. Guo, B.E.G. Lucier, W. Luo, M.S. Workentin, X. Sun, Y. Huang, Anhydride Post-Synthetic Modification in a Hierarchical Metal-Organic Framework, J Am Chem Soc 142 (2020) 4419–4428.

[4] C. Orellana-Tavra, M. Köppen, A. Li, N. Stock, D. Fairen-Jimenez, Biocompatible, Crystalline, and Amorphous Bismuth-Based Metal-Organic Frameworks for Drug Delivery, ACS Appl Mater Interfaces 12 (2020) 5633–5641.

[5] M.C. Wasson, C.T. Buru, Z. Chen, T. Islamoglu, O.K. Farha, Metal–organic frameworks: A tunable platform to access single-site heterogeneous catalysts, Appl Catal A Gen 586 (2019) 117214.

[6] I. Strauss, A. Mundstock, M. Treger, K. Lange, S. Hwang, C. Chmelik, P. Rusch, N.C. Bigall, T. Pichler, H. Shiozawa, J. Caro, Metal-Organic Framework Co-MOF-74-Based Host-Guest Composites for Resistive Gas Sensing, ACS Appl Mater Interfaces 11 (2019) 14175–14181.

[7] J. L. Segura, N. Martín, New Concepts in Tetrathiafulvalene Chemistry, Angewandte Chemie 40 (2001) 1372–1409.

[8] L. Liu, Y. Zhou, S. Liu, M. Xu, The Applications of Metal−Organic Frameworks in Electrochemical Sensors, Chem. Electro. Chem. 5 (2018) 6–19.

[9] K.J. Erickson, F. Léonard, V. Stavila, M.E. Foster, C.D. Spataru, R.E. Jones, B.M. Foley, P.E. Hopkins, M.D. Allendorf, A.A. Talin, Thin film thermoelectric metal-organic framework with high seebeck coefficient and low thermal conductivity, Advanced Materials 27 (2015) 3453–3459.

[10] Y. Ren, G.H. Chia, Z. Gao, Metal–organic frameworks in fuel cell technologies, Nano Today 8 (2013) 577–597.

[11] G. Xu, P. Nie, H. Dou, B. Ding, L. Li, X. Zhang, Exploring metal organic frameworks for energy storage in batteries and supercapacitors, Materials Today 20 (2017) 191–209.

[12] L.S. Xie, G. Skorupskii, M. Dincă, Electrically Conductive Metal–Organic Frameworks, Chem Rev 120 (2020) 8536–8580.

[13] R. Ricco, L. Malfatti, M. Takahashi, A.J. Hill, P. Falcaro, Applications of magnetic metal–organic framework composites, J Mater Chem A Mater 1 (2013) 13033–13045.

[14] J. Su, S. Yuan, H.Y. Wang, L. Huang, J.Y. Ge, E. Joseph, J. Qin, T. Cagin, J.L. Zuo, H.C. Zhou, Redox-switchable breathing behavior in tetrathiafulvalene-based metal–organic frameworks, Nature Communications 2017 8:1 8 (2017) 1–8.

[15] A. Altomare, M. C. Burla, M. Camalli, G. L. Cascarano, C. Giacovazzo, A. Guagliardi, A. G. G. Moliterni, G. Polidori, R. Spagna, SIR97: a new tool for crystal structure determination and refinement, J Appl Crystallogr 32 (1999) 115–119.

[16] G. M. Sheldrick, IUCr, A short history of SHELX, Acta Crystallogr 64 (2007) 112–122.

[17] L. J. Farrugia, IUCr, WinGX and ORTEP for Windows: an update, J Appl Crystallogr 45 (2012) 849–854.

[18] N. Benbellat, K.S. Gavrilenko, Y. le Gal, O. Cador, S. Golhen, A. Gouasmia, J.M. Fabre, L. Ouahab, Co(II)-Co(II) paddlewheel complex with a redox-active ligand derived from TTF., Inorg Chem 45 (2006) 10440–10442.

[19] A.W. Addison, T.N. Rao, J. Reedijk, J. Van Rijn, G.C. Verschoor, Synthesis, structure, and spectroscopic properties of copper(II) compounds containing nitrogen–sulphur donor ligands; the crystal and molecular structure of aqua[1,7-bis(N-methylbenzimidazol-2′-yl)-2,6-dithiaheptane]copper(II) perchlorate, Journal of the Chemical Society, Dalton Transactions (1984) 1349–1356.

[20] V. Amani, A New Imide-pyrazine Zinc(II) Binuclear Complex; In Situ Synthesis and Crystal Structure Determination, Inorganic Chemistry Research 6 (2022) 155–160.

[21] A. Klein, M. Neugebauer, A. Krest, A. Lüning, S. Garbe, N. Arefyeva, N. Schlörer, Five Coordinate Platinum(II) in [Pt(bpy)(cod)(Me)][SbF6]: A Structural and Spectroscopic Study, Inorganics 2015, Vol. 3, Pages 118-138 3 (2015) 118–138.

[22] A. Abedi, Z. Mehri-Lighvan, M. Yasan, V. Amani, Novel Cu(II) complexes of bithiazole: structure and biological study, Journal of the Iranian Chemical Society 14 (2017) 491–502.

[23] S. Kimura, H. Uchida, T. Kusamoto, H. Nishihara, One-dimensional magnetic chain composed of CuII and polychlorinated dipyridylphenylmethyl radical: temperature-dependent Jahn–Teller distortion correlated to π-conjugation and magnetic properties, Dalton Transactions 48 (2019) 7090–7093.

[24] W. Maalej, P. Guionneau, Z. Elaoud, A new square pyramidal copper(II) complex [Cu(C10H24N4)Br]Br: Crystal structure, thermal analysis, Hirschfeld surfaces, electrical and semiconducting properties, J Mol Struct 1241 (2021) 130630.

[25] N. Benbellat, Y. le Gal, S. Golhen, A. Gouasmia, L. Ouahab, Synthesis, characterization and X-ray structures of tetrathiafulvalene-type electron donors bearing one pyridine group, Synth Met 162 (2012) 1789–1797.

[26] M. Yang, J. Sun, J. Guo, G. Sun, L. Li, Cu–Ln compounds based on nitronyl nitroxide radicals: synthesis, structure, and magnetic and fluorescence properties, CrystEngComm 18 (2016) 9345–9356.

[27] J. Xie, J. Han, X. Huang, C. Jin, L. Li, J.P. Sutter, Enhancing the Magnetization Blocking Energy of Biradical-Metal System by Merging Discrete Complexes into One-Dimensional Chains, Chemistry – A European Journal 29 (2023) e202203852.

[28] R.A. Allão Cassaro, J.R. Friedman, P.M. Lahti, Copper(II) coordination compounds with sterically constraining pyrenyl nitronyl nitroxide and imino nitroxide, Polyhedron 117 (2016) 7–13.

[29] K. Maryunina, K. Yamaguchi, S. Nishihara, K. Inoue, G. Letyagin, G. Romanenko, I. Barskaya, S. Veber, M. Fedin, A. Bogomyakov, M. Petrova, V. Morozov, V. Ovcharenko, Intermolecular Spin-Crossover-like Phenomenon Sensitive to Applied External Pressure in Heterospin Crystals, Cryst Growth Des 20 (2020) 2796–2802.

[30] E. J. Baerends, T. Ziegler, A. J. Atkins, J. Autschbach, D. Bashford, A. Bérces, F. M. Bickelhaupt, C. Bo, P. M. Boerrigter, L. Cavallo, D. P. Chong, D. V. Chulhai, L. Deng, R. M. Dickson, J. M. Dieterich, D. E. Ellis, M. van Faassen, L. Fan, T. H. Fischer, C. Fonseca Guerra, M. Franchini, A. Ghysels, A. Giammona, S. J. A. van Gisbergen, A. W. Götz, J. A. Groeneveld, O. V. Gritsenko, M. Grüning, S. Gusarov, F. E. Harris, P. van den Hoek, C. R. Jacob, H. Jacobsen, L. Jensen, J. W. Kaminski, G. van Kessel, F. Kootstra, A. Kovalenko, M. V. Krykunov, E. van Lenthe, D. A. McCormack, A. Michalak, M. Mitoraj, S. M. Morton, J. Neugebauer, V. P. Nicu, L.

Noodleman, V. P. Osinga, S. Patchkovskii, M. Pavanello, C. A. Peeples, P. H. T. Philipsen, D. Post, C. C. Pye, W. Ravenek, J. I. Rodriguez, P. Ros, R. Rüger, P. R. T. Schipper, H. van Schoot, G. Schreckenbach, J. S. Seldenthuis, M. Seth, J. G. Snijders, M. Solà, M. Swart, D. Swerhone, G. te Velde, P. Vernooijs, L. Versluis, L. Visscher, O. Visser, F. Wang, T. A.Wesolowski, E. M. van Wezenbeek, G. Wiesenekker, S. K. Wolff, T. K. Woo, A. L. Yakovlev, ADF2022.103, SCM, Theoretical Chemistry, Vrije Universiteit, Amsterdam, The Netherlands, http://www.scm.com., (n.d.).

[31] J.P. Perdew, K. Burke, M. Ernzerhof, Generalized Gradient Approximation Made Simple, Phys Rev Lett 78 (1997) 1396.

[32] G. Scalmani, M.J. Frisch, B. Mennucci, J. Tomasi, R. Cammi, V. Barone, Geometries and properties of excited states in the gas phase and in solution: Theory and application of a time-dependent density functional theory polarizable continuum model, J Chem Phys 124 (2006) 094107.

[33] O.V. Gritsenko, P.R.T. Schipper, E.J. Baerends, Ensuring proper short-range and asymptotic behavior of the exchange-correlation Kohn-Sham potential by modeling with a statistical average of different orbital model potentials, Int J Quantum Chem 76 (2000) 407–419.

[34] M. Kohout, DGrid, DGrid, Version 4.3, Radebeul (n.d.).

[35] Chemcraft - graphical software for visualization of quantum chemistry computations. https://www.chemcraftprog.com, Chemcraft - Graphical Software for Visualization of Quantum Chemistry Computations. https://www.chemcraftprog.com (n.d.).

[36] F.L. Hirshfeld, Bonded-atom fragments for describing molecular charge densities, Theoretica Chimica Acta 1977 44:2 44 (1977) 129–138.

[37] C.F. Matta, J. Hernández-Trujillo, T.H. Tang, R.F.W. Bader, Hydrogen–Hydrogen Bonding: A Stabilizing Interaction in Molecules and Crystals, Chemistry – A European Journal 9 (2003) 1940–1951.

[38] A. Martín Pendás, E. Francisco, M.A. Blanco, C. Gatti, Bond Paths as Privileged Exchange Channels, Chemistry – A European Journal 13 (2007) 9362–9371.

[39] S.J. Grabowski, A. Pfitzner, M. Zabel, A.T. Dubis, M. Palusiak, Intramolecular H,,,H Interactions for the Crystal Structures of [4-((E)-But-1-enyl)-2,6-dimethoxyphenyl]pyridine-3-carboxylate and [4-((E)-Pent-1-enyl)-2,6-dimethoxyphenyl]pyridine-3-carboxylate; DFT Calculations on Modeled Styrene Derivatives, (2004).

[40] R.F.W. Bader, H. Essén, The characterization of atomic interactions, J Chem Phys 80 (1998) 1943.

[41] R.G.A. Bone, R.F.W. Bader, Identifying and analyzing intermolecular bonding interactions in van der Waals molecules, Journal of Physical Chemistry 100 (1996) 10892–10911.

[42] E. Espinosa, I. Alkorta, J. Elguero, E. Molins, From weak to strong interactions: A comprehensive analysis of the topological and energetic properties of the electron density distribution involving X–H···F–Y systems, J Chem Phys 117 (2002) 5529.

[43] S. Uzun, Z. Esen, E. Koç, N.C. Usta, M. Ceylan, Experimental and density functional theory (MEP, FMO, NLO, Fukui functions) and antibacterial activity studies on 2-amino-4- (4-nitrophenyl) -5,6-dihydrobenzo [h] quinoline-3-carbonitrile, J Mol Struct 1178 (2019) 450–457.

[44] T. Koopmans, Über die Zuordnung von Wellenfunktionen und Eigenwerten zu den Einzelnen Elektronen Eines Atoms, Physica 1 (1934) 104–113.

[45] P. Hobza, J. Řezáč, Introduction: Noncovalent Interactions, Chem Rev 116 (2016) 4911–4912.

[46] E. R. Johnson, S. Keinan, P. Mori-Sánchez, J. Contreras-García, A. J. Cohen, W. Yang, Revealing Noncovalent Interactions, J Am Chem Soc 132 (2010) 6498–6506.

[47] E. Scrocco, J. Tomasi, Electronic Molecular Structure, Reactivity and Intermolecular Forces: An Euristic Interpretation by Means of Electrostatic Molecular Potentials, Advances in Quantum Chemistry 11 (1978) 115–193.

[48] J. Andres, S. Berski, J. Contreras-Garcia, P. Gonzalez-Navarrete, Following the molecular mechanism for the NH3+ LiH→ LiNH2+ H2 chemical reaction: a study based on the joint use of the quantum theory of atoms in molecules (QTAIM) and noncovalent interaction (NCI) index, J Phys Chem A 118 (2014) 1663–1672.

[49] J. Contreras-García, R.A. Boto, F. Izquierdo-Ruiz, I. Reva, T. Woller, M. Alonso, A benchmark for the non-covalent interaction (NCI) index or… is it really all in the geometry?, Theoretical Chemistry Accounts 2016 135:10 135 (2016) 1–14.

[50] H. Chermette, Chemical reactivity indexes in density functional theory, J Comput Chem 20 (1999) 129–154.

[51] R. G. Parr, R. A. Donnelly, M. Levy, W. E. Palke, Electronegativity: The density functional viewpoint, J Chem Phys 68 (2008) 3801.

[52] R.G. Parr, L. v. Szentpály, S. Liu, Electrophilicity index, J Am Chem Soc 121 (1999) 1922–1924.

[53] R.G. Parr, W. Yang, Density functional approach to the frontier-electron theory of chemical reactivity, J Am Chem Soc 106 (2002) 4049–4050.

[54] K. Fukui, Role of frontier orbitals in chemical reactions on JSTOR, Science (1979) 218 (1982) 747–754.

[55] T. Ziegler, A. Rauk, On the calculation of bonding energies by the Hartree Fock Slater method, Theor Chim Acta 46 (1977) 1–10.

[56] T. Lu, F. Chen, Quantitative analysis of molecular surface based on improved Marching Tetrahedra algorithm, Journal of Molecular Graphics and Modelling 38 (2012) 314–323.

[57] H. Ghanem, O. Khaoua, A. Ouahab, N. Benbellat, H. Haba, *In silico* Pharmacodynamics, Antineoplastic Activity and Molecular Docking of two Phytochemicals Isolated from Thymelaea microphylla, Lett Drug Des Discov 20 (2023) 1–17.

[58] J. Coates, Interpretation of Infrared Spectra, A Practical Approach, n.d.

[59] R. Bozio, A. Girlando, D. Pecile, Infrared and Raman spectra of TTF and TTF-d4, Chem Phys Lett 52 (1977) 503–508.

[60] D. N. Sathyanarayana, Vibrational Spectroscopy-theory and Applications, 2nd ed., New Age International (P) Limited Publishers, New Delhi, 2004.

[61] O. Khaoua, S. Mouffouk, N. Benbellat, S. Zeroual, S. Golhen, A. Gouasmia, H. Chermette, H. Haba, Synthesis, Characterisation, Hirshfeld surface analysis, Magnetic susceptibility, DFT calculations, pkCSM profile, and Biological activities of Novel mono-, di-, and multinuclear Cobalt (II) complexes, Eur J Inorg Chem (2024) e202400033.

[62] O. Khaoua, N. Benbellat, S. Zeroual, S. Mouffouk, S. Golhen, A. Gouasmia, H. Chermette, H. Haba, Combined experimental, computational studies (synthesis, crystal structural, DFT calculations, spectral analysis) and biological evaluation of the new homonuclear complex Di-μ-benzoato-bis [benzoatodipyridine-cobalt (II)], J Mol Struct 1273 (2023) 134331.

[63] S. Belhouchat, S. Zeroual, N. Benbellat, O. Khaoua, S. Bouchekioua, R. Menacer, H. Chermette, DFT and Docking Calculations of the Structural, Electronic, Biological and Conductivity Properties of the Synthetic Complex [Cu(hfac)2(L)2][PF6]2, ChemistrySelect 9 (2024) e202304155.

[64] L. Gasque, G. Medina, L. Ruiz-Ramírez, R. Moreno-Esparza, Cu–O stretching frequency correlation with phenanthroline pKa values in mixed copper complexes, Inorganica Chim Acta 288 (1999) 106–111.

[65] J. Santos, B. Grimm, B.M. Illescas, D.M. Guldi, N. Martín, Cooperativity between π–π and H-bonding interactions–a supramolecular complex formed by C60 and exTTF, Chemical Communications (2008) 5993–5995.

[66] S.S. Gayathri, M. Wielopolski, E.M. Pérez, G. Fernández, L. Sánchez, R. Viruela, E. Ortí, D.M. Guldi, N. Martín, Discrete Supramolecular Donor–Acceptor Complexes, Angewandte Chemie International Edition 48 (2009) 815–819.

[67] E.M. Pérez, A.L. Capodilupo, G. Fernández, L. Sánchez, P.M. Viruela, R. Viruela, E. Ortí, M. Bietti, N. Martín, Weighting non-covalent forces in the molecular recognition of C60. Relevance of concave–convex complementarity, Chemical Communications (2008) 4567–4569.

[68] B.M. Illescas, J. Santos, M. Wielopolski, C.M. Atienza, N. Martín, D.M. Guldi, Electron transfer through exTTF bridges in electron donor–acceptor conjugates, Chemical Communications (2009) 5374–5376.

[69] I.D. Petsalakis, D. Tzeli, I.S.K. Kerkines, G. Theodorakopoulos, Theoretical study on the electronic structure and the absorption spectra of complexes of C60 and C59N with π-extended derivatives of tetrathiafulvalene, Comput Theor Chem 965 (2011) 168–175.

[70] A. Midoune, A. Messaoudi, DFT/TDDFT studies of the structural, electronic and NBO properties of some complexes with the tetrathiafulvalene-1,3-benzothiazole ligand, Inorganica Chim Acta 516 (2021) 120151.

Declaration of interests

☒The authors declare that they have no known competing financial interests or personal relationships that could have appeared to influence the work reported in this paper.

☐The authors declare the following financial interests/personal relationships which may be considered as potential competing interests:

Graphical abstract